Normal modes and their librations at the outer edge of Saturn's B Ring, as observed in Cassini stellar and radio occultation data

Richard G French, Philip D Nicholson, Colleen A Mcghee-French, Pierre-Yves Longaretti, Matthew M Hedman, Joshua Colwell, Essam A Marouf, Nicole Rappaport, Sophia Flury, Jolene Fong, et al.

Draft version January 16, 2023
Typeset using LaTeX **modern** style in AASTeX631

Normal modes and their librations at the outer edge of Saturn's B Ring, as observed in Cassini stellar and radio occultation data (v2.3)

Richard G. French,[1] Philip D. Nicholson,[2] Colleen A. McGhee-French,[1] Pierre-Yves Longaretti,[3] Matthew M. Hedman,[4] Joshua Colwell,[5] Essam A. Marouf,[6] Nicole Rappaport,[7] Sophia Flury,[8] Jolene Fong,[1] Ryan Maguire,[9] and Glen Steranka[1]

[1]*Department of Astronomy, Wellesley College, Wellesley, MA 02481*
[2]*Department of Astronomy, Cornell University, Ithaca, NY 14853*
[3]*Institut de Planétologie et d'Astrophysique de Grenoble, Grenoble, FR*
[4]*Department of Physics, University of Idaho, Moscow, ID 83844*
[5]*Department of Physics, University of Central Florida, Orlando, FL 32816*
[6]*Department of Electrical Engineering, San José State University, San José, CA 95192*
[7]*Jet Propulsion Laboratory, Pasadena, CA 91109 (retired)*
[8]*Department of Astronomy, University of Massachusetts, Amherst, MA 01003*
[9]*Department of Mathematics, Dartmouth College, Hanover, NH 03755*

ABSTRACT

We redetermine the time-variable shape of the outer edge of Saturn's B ring using the complete set of *Cassini* radio and stellar occultation data obtained between mid-2005 and the End-of-Mission in late 2017, considerably expanding the range and number of individual ring edge measurements used in our previous analysis (Nicholson, P. D. et al. [2014] Icarus 227,152-175). During this 12-year interval, the dominant $m = 2$ pattern driven by the Mimas 2:1 inner Lindblad resonance completed just over two slow prograde circulations relative to Mimas, at an angular frequency of $\Omega_L = 0.1838 \pm 0.0006^\circ$ d^{-1} (corresponding to a period of 5.362 ± 0.017 yr). At the same time, the radial amplitude of this pattern varied from a minimum of ~ 4 km to a maximum of ~ 71 km, due to beating between the forced and free $m = 2$ components originally identified by Spitale, J. and Porco, C. [2010] (Astron. J. 140, 1747-1757). This circulation pattern has remained essentially unchanged when compared with previous studies based on *Cassini* imaging and occultation data sets acquired prior to 2012 (Spitale and Porco 2010; Nicholson et al. 2014a). On the other hand, we find strong evidence for significant time variability in the four additional perturbations seen at the B ring edge with azimuthal wavenumbers $m = 1$, 3, 4 and 5. These non-resonant perturbations have previously been interpreted as normal (or edge) modes

Corresponding author: Richard G. French
rfrench@wellesley.edu

that exist in relatively narrow cavities adjacent to the ring edge, perhaps triggered by viscous overstabilities (see reviews by Longaretti (2018) and Nicholson et al. (2018)). The $m = 1$ perturbation, which rotates at the local apsidal precession rate, decreased in radial amplitude from ∼25 km in 2005 to ∼20 km in 2008/09, but subsequently increased to ∼30 km in 2013, before falling back to ∼17 km in 2016/17. These variations can be modeled as a libration in the eccentricity of the ring's streamlines involving two independent modes with periods of 8.6 and 5.9 yr and amplitudes of 4.4 and 2.8 km, respectively. Similar variability in the amplitude of the $m = 3$ perturbation from a minimum of ~ 6 km to a minimum of ~ 20 km can be modeled in terms of librations with periods of 19.7 and 7.3 yr and amplitudes of 7.4 and 2.2 km, respectively. Smaller but still significant variations are seen in the amplitudes of the $m = 4$ and $m = 5$ modes, with periods of 2.3 – 5.9 yr and amplitudes of 1.6 – 2.8 km. We present libration models for all four non-resonant perturbations, fitted to the Cas occultation data, but the physical interpretation of these models is uncertain. Theoretical modeling by **?** suggests that the observed amplitude variations could represent (1) interference between multiple normal modes with the same value of the azimuthal wavenumber m but different numbers of radial nodes n_r, (2) a periodic oscillation in the amplitude of a single normal mode with $n_r = 0$ (known as the 'nodeless mode'), or (3) nonlinear coupling between normal modes with different values of m, leading to long-term aperiodic variatiuions in the mode amplitudes. On the assumption that model (1) is correct, we use the observed oscillation and libration frequencies of the modes to estimate the surface mass density in the outer $\sim$ 1200 km of the B ring, finding values ranging from 50 g cm^{-2} to $\sim$ 250 g cm^{-2}. **These numbers & text need to be revised!**

Keywords: occultations, planets: rings; dynamics

1. INTRODUCTION

The outer edge of Saturn's B ring — which is also the inner edge of the Cassini Division — coincides with the strongest satellite resonance in the rings, the 2:1 inner Lindblad resonance with Mimas (**?**). Although the likely connection between satellite resonances and the location of the Cassini Division was recognized in the 19th century (Kirkwood 1866), if not earlier, the modern understanding of this phenomenon is due to Goldreich and Tremaine (1978), who pointed out that the torque exerted by Mimas on the ring at this resonance is probably large enough to counteract the outward transport of angular momentum through the B ring due to viscous interactions between the ring particles. As a result, the ring material is prevented from spreading radially beyond the resonance, and the edge of the B ring is effectively

held in balance. A consequence of this picture is that Mimas should force significant perturbations on the orbits of ring particles near the resonance, resulting in a 2-lobed radial pattern that is expected to rotate at the same angular velocity as the satellite, or approximately one-half of the local Keplerian rate. Such a perturbation was in fact observed in *Voyager* observations of the rings in 1980/81 (Porco et al. 1984), where it was found to agree fairly well with theoretical expectations: at that time, the observed radial amplitude of the ring edge was ∼75 km and one of the two radial minima was found to be aligned with Mimas to within a few degrees. The torque itself, like the tidal torque exerted on the Earth's rotation by the Moon, arises from the interaction between this radial distortion of the ring streamlines and the gravitational potential of Mimas, and thus scales as the square of Mimas's mass. It is also proportional to the small phase lag in the ring's response relative to Mimas. For a recent discussion of the dynamics involved, as well as several as-yet-unanswered questions about this process, the reader is directed to the review by Longaretti (2018).

A similar situation occurs in the A ring, where another strong resonance appears to confine the outer edge of the ring against a similar tendency to spread radially. Here, the basic pattern observed is a 7-lobed radial perturbation due to the 7:6 inner Lindblad resonance with Janus (Porco et al. 1984). In this case, however, the satellite involved is well-known to share a common mean orbit with its smaller sibling Epimetheus (Yoder et al. 1989). The 4-year coorbital libration significantly complicates the situation, leading to a time-dependent interaction between the satellite and the ring edge (Lissauer et al. 1985; El Moutamid et al. 2016; Nicholson et al. 2022) A revised calculation of the overall torque balance for both the A and B rings, taking into account the effects of many additional satellite resonaces, was made by Tajeddine et al. (2017), leading to updated estimates of the radial viscosity profiles across both rings.

With the advent of data from the *Cassini* spacecraft, it became possible to revisit the question of the shapes of the outer edges of the A and B rings, and to characterize them with much greater fidelity than was possible with the more limited *Voyager* observations. This problem was tackled using azimuthal mosaics of images acquired with *Cassini*'s Imaging Science Subsystem (ISS) during the initial years of the mission and by combining data from several dozen radio and stellar occultations observed by the Radio Science Subsystem (RSS) and the Visual and Infrared Imaging Spectrometer (VIMS). Spitale and Porco (2009) used ISS data to study the shape of the A ring's outer edge, while that of the B ring was analyzed by Spitale and Porco (2010), based on data taken between 2005 and 2009. Hedman et al. (2010) investigated the kinematics of the B ring edge using VIMS occultations between 2005 and 2008, while French et al. (2010) carried out a similar study using a smaller set of RSS occultations from 2005.

As a result of these investigations, it was established that the shape of the B ring's edge, in particular, is remarkably complex. There are not one but two 2-lobed patterns, with similar radial amplitudes of approximately 35 km but rotating at slightly different angular rates. The slower of the two modes is that forced by Mimas, while the faster is a free, or 'normal' mode (see below). The result is that the two patterns beat against one another, alternately adding constructively and then almost cancelling each other out (Hedman et al. 2010). Fits to a somewhat longer span of *Cassini* occultation data showed that the beat period is 5.42 yrs, with the overall $m = 2$ amplitude reaching a maximum of 71 km and a minimum of 3 km (Nicholson et al. 2014a). During this cycle, the $m = 2$ pattern was actually found to rotate through 360° relative to Mimas, instead of remaining aligned with the satellite as had been predicted (Spitale and Porco 2010). Radial minima are anti-aligned with Mimas at the times of minimum amplitude, which occurred during the *Cassini* mission in 2006.80, 2012.24 and 2017.69. In addition to this circulating $m = 2$ pattern, there is a slowly-rotating $m = 1$ perturbation (equivalent to a precessing Keplerian ellipse) with an amplitude of ∼20 km and a rapidly-rotating $m = 3$ pattern with an amplitude of ∼10 km. Evidence was later found for smaller-amplitude patterns with $m = 4$ and $m = 5$ (Nicholson et al. 2014a). These non-resonant perturbations with $m = 1$, 3, 4 and 5, as well as the free mode with $m = 2$, are thought to represent normal modes trapped in resonant cavities near the ring's edge (Spitale and Porco 2010; Nicholson et al. 2018).

In the present paper we return to the question of the shape of the B ring's outer edge, now armed with the complete set of *Cassini* radio and stellar occultation data obtained between mid-2005 and the End-of-Mission in late-2017. In addition to data from the RSS and VIMS experiments, we use stellar occultation data obtained by the Ultraviolet Imaging Spectrometer (UVIS), for a total of 294 measurements. Our goals are: (i) to characterize the forced $m = 2$ mode and its phase lag relative to Mimas, with the hope of testing the resonantconfinement model of Goldreich and Tremaine (1978), (ii) to better establish the parameters and character of the normal modes with $m = 1$, 2, 3, 4 and 5, and (iii) to search for additional, weaker perturbations that may shed further light on how this complex region works.

In a separate paper (Nicholson et al. 2022) we have carried out a similar investigation of the outer edge of the A ring, using the same occultation data set.

The layout of the paper is as follows. In Section 2 we outline the dynamical model used to fit the occultation data, which are themselves summarized in Section 3. The numerical codes used for orbit fitting and frequency scanning are reviewed in Section 4. In Section 5 we update the fits published by Nicholson et al. (2014a), using the expanded *Cassini* data set. Our new results are presented in Section 6, and we summarize our key findings and open questions in Section 7.

2. DYNAMICAL MODEL

Underlying all of the orbital fits in this paper is a common kinematic model for an m-lobed radial perturbation, appropriate to both a Lindblad resonance due to an external satellite and to free normal modes of oscillation. Our notation follows closely that used in our previous papers, in particular Nicholson et al. (2014a), Nicholson et al. (2014b) and French et al. (2016), so that the fit parameters obtained here may be compared directly with the corresponding values given there. The radial perturbation in a ring streamline due to such a mode can be written as a function of inertial longitude λ and time t in the form

$$\Delta r(m, \lambda, t) = -A_m \cos(m[\lambda - \Omega_P(t - t_0) - \delta_m]), \tag{1}$$

where A_m and δ_m are the mode's radial amplitude and phase, respectively, and Ω_P is its angular rotation rate or pattern speed. Geometrically, the angle δ_m is the inertial longitude of one of the pattern's m minima at the reference time t_0. In the residual plots shown below we use the corotating longitude $\theta = \lambda - \Omega_P(t - t_0) - \delta_m$, so the angular argument becomes simply $m\theta$. For a freely-precessing normal mode, the pattern speed is expected to be very close to that of a first-order $m : m-1$ Lindblad resonance located at the mean radius of the streamline (French et al. 1991), or

$$\Omega_P = [(m-1)n + \dot{\varpi}_{\rm sec}]/m, \tag{2}$$

where n is the local orbital angular velocity and $\dot{\varpi}_{\rm sec}$ is the local apsidal precession rate due to the planet's zonal gravity harmonics.[1] In general, the integer m can be either positive or negative, corresponding to ILR-type modes with $\Omega_P < n$ or OLR-type modes with $\Omega_P > n$, respectively. (This terminology refers to an inner or outer Lindblad resonance, which the normal mode perturbations strongly resemble.) The former are expected to occur at the outer edges of rings, whereas the latter should be found at inner edges, as discussed in Nicholson et al. (2014b) and French et al. (2016) and reviewed by Nicholson et al. (2018). At the outer edge of the B ring, only ILR-type modes are expected (*i.e.,* $m > 0$). A normal mode with $m = 1$ is equivalent to a freely-precessing Keplerian ellipse, with $\Omega_P = \dot{\varpi}_{\rm sec}$, the apsidal precession rate and $\delta_1 = \varpi_0$, the longitude of pericenter at $t = t_0$.

In the case of perturbations by an external satellite, Ω_P is determined by the relevant term in the satellite's gravitational potential. For the B ring edge, the resonant perturbations are due to the Mimas 2:1 inner Lindblad resonance for which $m = 2$ and $\Omega_P = n_{\rm Mimas}$. Here, we expect that $\delta_2 = \lambda^0_{\rm Mimas}$, the mean longitude of Mimas at $t = t_0$, although in our fits we allow for a small offset $\delta\lambda$ to account for the anticipated phase lag between the radial minimum and the direction towards the satellite. (A positive value of $\delta\lambda$ means that the radial minimum *leads* Mimas in longitude.)

[1] Expressions for n and $\dot{\varpi}_{\rm sec}$ accurate to order J_6 are given by Nicholson et al. (2014b), Eqns. (3–8) and Nicholson et al. (2018), Eqns. (26 & 27).

In the current paper, we shall also be concerned with modes whose amplitude and phase oscillate, or *librate* about their average values. In this situation we generalize Eq. (1) to the form

$$\begin{aligned}\Delta r(m,\lambda,t) &= -A_m\,\cos(m\theta-\phi_L)\\ &= -A_m\,\cos(m[\lambda-\Omega_P(t-t_0)-\delta_m]-\phi_L),\end{aligned} \tag{3}$$

where both A_m and ϕ_L are slowly-varying functions of time. Following the standard model used to describe secular perturbations of asteroid or satellite orbits (Murray & Dermott 1999), or that introduced by Hedman et al. (2010) and Spitale and Porco (2010) to describe resonant librations associated with the Mimas 2:1 ILR, we write $A_m = ae$ and describe these periodically-varying parameters in terms of the Cartesian quantities $h = e\,\cos(\phi_L)$ and $k = e\,\sin(\phi_L)$ via the expressions

$$\begin{aligned}h &= e_0+e_1\,\cos[\Omega_L(t-t_0)-\delta_L]\\ k &= e_1\,\sin[\Omega_L(t-t_0)-\delta_L],\end{aligned} \tag{4}$$

where e_0 and e_1 are constants, Ω_L is the libration frequency and δ_L is a constant specifying the phase of the libration.[2] Geometrically, the vector (h,k) moves around a circle of radius e_1 at an angular rate Ω_L, with the center of the circle offset from the origin by an amount e_0 along the $+h$-axis. In the context of secular or resonant perturbations, e_0 is referred to as the forced eccentricity and e_1 as the free or proper eccentricity. In the present situation, ae_0 and ae_1 simply represent the average and variable components of the mode's amplitude A_m. In terms of $h(t)$ and $k(t)$, the instantaneous values of e and ϕ_L are given by

$$\begin{aligned}e &= \sqrt{h^2+k^2}\\ \phi_L &= \tan^{-1}(k/h).\end{aligned} \tag{5}$$

Similar expressions are given by Hedman et al. (2010) in Eqns. (35–40) and by Spitale and Porco (2010) in Eqns. (6 & 11); see also Fig. 4 in Spitale and Porco (2010) for a graphical representation of the motion. From Eq. (4) we see that the mode amplitude $A_m = ae$ is a maximum when the angle $\Omega_L(t-t_0)-\delta_L$ is zero, or when

$$t - t_0 = \delta_L/\Omega_L + 2\pi k/\Omega_L, \tag{6}$$

where k is any integer.

As shown by Spitale and Porco (2010), such a model for a librating streamline is mathematically equivalent to a superposition of two independent normal modes with the same value of m, radial amplitudes ae_0 and ae_1 and slightly different pattern speeds Ω_0 and Ω_1. Geometrically, one may imagine two independent normal modes,

[2] For simplicity, we refer to this motion as libration, implying an oscillation in ϕ_L, but this can also include the case where $e_1 > e_0$, when the angle ϕ_L actually circulates continuously through 360°.

one with amplitude ae_0 rotating at a rate Ω_0 and the other with amplitude ae_1 and angular frequency Ω_1, combining to produce a single, pulsating, rotating perturbation with a beat frequency equal to $|m(\Omega_1 - \Omega_0)|$ and an amplitude that varies from a minimum of $a|e_0 - e_1|$ to a maximum of $a(e_0 + e_1)$. We then somewhat arbitrarily choose $\Omega_P = \Omega_0$ and the corresponding libration frequency is given by

$$\Omega_L = m(\Omega_1 - \Omega_0). \tag{7}$$

(The factor of m arises because each mode has m radial minima and maxima.)

There are thus two dynamically-distinct scenarios that can arise, one in which a single mode oscillates in amplitude and phase and the other in which two stable modes with the same value of m and similar pattern speeds interfere to produce a beating pattern. In the first case we might have a single mode whose amplitude and phase vary due to a viscous overstability as originally envisioned by Borderies et al. (1985), while in the second case we might have two independent edge modes with the same m but different numbers of radial nodes and thus slightly different pattern speeds (Longaretti 2018). These two scenarios are indistinguishable when only the shape of a single ring streamline — such as a ring edge — is analyzed. But if the radial distribution of eccentricity across the perturbed region of the ring could be assessed, and its temporal variation established, then these two situations would look quite different. We will return to this issue in the Discussion.

For some values of m we have found it necessary to introduce additional librational terms, replacing Eq. (4) by the more general expression:

$$\begin{aligned} h = \;& e_0 + \sum_{j=1}^{n} e_j \;\cos[\Omega_{L,j}(t - t_0) - \delta_{L,j}] \\ k = \;& \sum_{j=1}^{n} e_j \;\sin[\Omega_{L,j}(t - t_0) - \delta_{L,j}] \end{aligned} \tag{8}$$

where each librational term has its own frequency $\Omega_{L,j}$ and phase $\delta_{L,j}$. **Figure 1** illustrates the overall eccentricity and phase for a mode with two libration terms, plotted in (h, k) space. The radial line from the origin to the center of the larger circle of length e_0 is fixed, while the radius vectors of the two smaller circles (labeled e_1 and e_2) rotate at angular rates of $\Omega_{L,1}$ and $\Omega_{L,2}$, respectively. (Note that this diagram shows just the variation in amplitude e and phase ϕ_L of the mode, rather than the shape of the ring streamline itself, which is an m-lobed figure, or its orientation relative to inertial space as controlled by Ω_P and δ_m.

In general, a particular ring streamline may be perturbed simultaneously by several different normal modes, each with its own value of the azimuthal wavenumber m, and each of these modes can librate with one or more components, following Eq. (8). Such

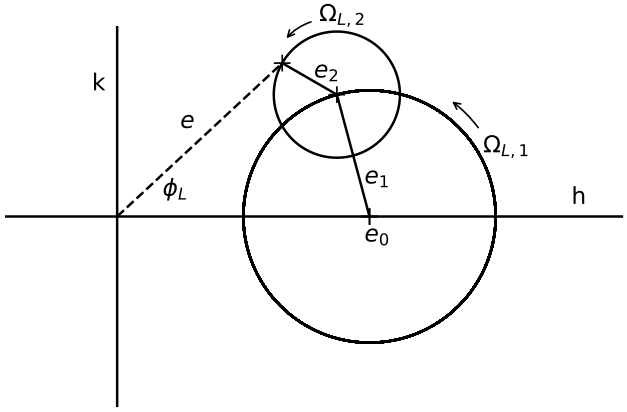

Figure 1. Illustration of the time-varying eccentricity vector $\{h, k\}$ for a mode with two libration terms and a mean amplitude ae_0. The two smaller circles have radii of e_1 and e_2 and rotate at angular rates of $\Omega_{L,1}$ and $\Omega_{L,2}$, respectively. The instantaneous amplitude and phase of the mode are indicated by the dashed line and specified by ae and ϕ_L. (Adapted from Spitale and Porco (2010), Fig. 4.)

a model is specified by a set of free parameters given by the mean radius a, three parameters for the mean amplitude and phase for each mode (ae_0, Ω_P, δ_m) and an additional three parameters for each libration (ae_j, $\Omega_{L,j}$, $\delta_{L,j}$). A particular mode has m lobes of radial amplitude $A_m(t) = ae(t)$ with radial minima located at longitudes of

$$\lambda_{\min}(t) = \Omega_P(t - t_0) + \delta_m + \phi_L(t)/m + 2\pi k/m, \tag{9}$$

where $0 \leq k \leq m - 1$. Physically, the pattern has a mean amplitude ae_0 and rotates relative to inertial space at a mean rate Ω_P, while oscillating in both amplitude and orientation at a frequency (or frequencies) Ω_L.

3. OBSERVATIONS

The data used for this study come from a large set of *Cassini* ring occultations observed over the full course of the spacecraft's 2004–2017 orbital tour of the Saturn system. Details of the relevant VIMS, UVIS, and pre-2012 RSS occultation observations are provided in Nicholson et al. (2014a,b) and French et al. (2010, 2016, 2017), and are not repeated here. A total of 305 measurements of the B ring edge radius were included, with 58 from RSS, 115 from VIMS and 132 from UVIS. Fully calibrated versions of the occultation data are available from NASA's Planetary Data System (PDS) Ring-Moon Systems Node.[3]

[3] `https://pds-rings.seti.org/`

3.1. *Post-2011 RSS ring occultations*

In addition to the above data sets, we have included post-2011 RSS occultation results that contributed significantly to the final tally of B ring measurements used for this work, and these deserve more detailed discussion.

Unlike stellar occultation observations, which require only modest processing from their raw form to obtain useful science results, raw RSS ring occultation observations are strongly affected by diffraction effects that must by removed in order to determine the intrinsic optical depth profiles of the rings (Marouf et al. 1986). The diffraction reconstruction relies on a highly accurate measurement of the radio signal's phase, which requires a very stable transmitted frequency from the spacecraft. In late 2011, the *Cassini* spacecraft's ultrastable oscillator (USO) failed, and the auxiliary onboard oscillator had inadequate frequency stability to allow for accurate diffraction reconstruction of ring occultations. Instead, a novel mode of two-way RSS occultation experiments was implemented in 2012. Rather than depending on a stable onboard frequency source for the spacecraft's transmitted signal, an uplink radio signal from an Earth-based Deep Space Network (DSN) antenna was transmitted to the spacecraft, where it was phase-locked, amplified and then retransmitted to the ground, preserving the hydrogen maser-based frequency stability of the original signal from the DSN.

A key complication is that the uplinked signal passed through the rings on the way to the spacecraft, resulting in a phase distortion preserved in the downlink signal. In effect, the observations retain a "double exposure" or "phase echo" associated with the diffraction pattern of the ring region traversed by the uplink signal, coadded to the diffraction phase of the downlink signal. This contamination of the final received phase during an RSS occultation experiment similarly affects atmospheric occultations, but in this case the use of multi-frequency observations can correct for the phase distortion and enable accurate retrieval of the vertical profile of the atmospheric structure (Schinder et al. 2015).

For ring occultations, on the other hand, no general solution has yet been found to remediate the phase contamination that often results in badly distorted diffraction-corrected radial optical depth ring profiles. Under special circumstances, however, the observed diffraction pattern of specific ring features may be relatively unaffected by the uplink phase distortion. For example, it is possible to retrieve the intrinsic optical depth profile of an isolated narrow ringlet such as the F ring if the phase echo is sufficiently radially removed from the main diffraction signature of the downlink signal.

It is also possible, under the right geometric circumstances, to reconstruct the intrinsic sharp edge of a nearly opaque ring bounded by free space, such as the outer

edges of the A and B rings. Fortunately, a significant fraction of the post-2011 RSS occultations had such favorable geometry. In the end, we were able to apply standard diffraction-reconstruction techniques (Marouf et al. 1986) to process the X-band (3.6 cm wavelength) observations at 1-km effective resolution and to obtain accurate measurements of the B ring outer edge from 24 of 41 post-USO-failure RSS occultations that intersected the B ring, expanding the available data for the post-2011 period of the *Cassini* orbital tour.

3.2. *Measuring the location of the B ring edge*

As in our previous studies, we have included only high-SNR events with spatial resolution of 1 km or better that could be mapped onto an absolute radius scale with sub-km accuracy. For each such occultation that included the outer edge of the B ring, we fitted a logistic model curve to the edge profile to determine the midtime of the sharp-edged event. Using a Saturn ring orbit model similar to Fit #1 in French et al. (2017) but augmented to include the full set of 2005–2017 *Cassini* occultation data, we determined the orbital radius, inertial longitude, and ring plane intercept time of each B ring edge measurement. These represent the fundamental observables for our B ring orbit fits. The typical uncertainty in an individual radius determination, including systematic effects, is well below 1 km. Post-fit RMS residuals of ~ 5 km for our best B ring model fits greatly exceed this measurement uncertainty, and instead probably stem from complexities in the intrinsic shape of the B ring edge that are not captured by our kinematical models.

From preliminary orbit fits that included normal modes for $m = 1$ through 5 and the $m = 2$ mode forced by Mimas, we identified 11 of the 305 individual data points as having unacceptably large (> 20 km) post-fit residuals, corresponding to $\sim$4 standard deviations. Such outliers were a characteristic of our earlier B ring investigation (Nicholson et al. 2014a) and were also noted by Spitale and Porco (2010) in their analysis of imaging mosaics. They interpreted these large but localized radial disturbances in the B ring edge as evidence for the presence of massive bodies embedded within the B ring itself. We excluded this small number of outliers from our final data set because they unduly inflated the formal errors of the final fit parameters. The total number of data points used in our current fits is thus 294, or more than twice the 133 B ring edge measurements used by Nicholson et al. (2014a) .

4. ORBIT DETERMINATION

As in Nicholson et al. (2014a), we determine the best-fitting orbit model for the B ring edge using a straightforward and well-tested non-linear least squares procedure that minimizes the sum of squared differences between the observed and model radii, $r_{\rm obs}(\lambda, t)$ and $r_{\rm mod}(\lambda, t)$, where

Table 1. Omitted measurements of the B ring edge with large post-fit residuals.

Occultation	UTC (observed)	$r_{\rm obs}$ (km)	$r_{\rm model}$ (km)	dr (km)	λ (deg)
RSS_013E_X14	2005 AUG 20 20:37:46.8732	117569.19	117548.78	20.40	79.57
UVIS_EpsCen065I	2008 APR 19 11:32:19.8837	117551.54	117518.50	33.04	204.26
VIMS_alpAur110E	2009 MAY 09 16:45:55.8991	117583.65	117614.00	-30.35	243.49
RSS_180I_X14_65	2013 JAN 31 13:48:24.4050	117585.38	117557.22	28.16	299.28
VIMS_2Cen194E	2013 JUL 08 21:30:05.0270	117555.40	117585.98	-30.57	248.19
RSS_196I_X65_65	2013 AUG 08 18:24:19.3052	117584.64	117545.15	39.49	228.88
UVIS_AlpVir211I	2015 JAN 08 03:50:58.4312	117598.84	117627.00	-28.16	168.48
VIMS_alpSco238I	2016 JUL 19 13:45:57.5389	117557.58	117584.09	-26.51	233.76
RSS_236E_X43_14	2016 JUN 06 10:42:10.8061	117566.38	117594.51	-28.13	109.65
RSS_253E_X14_63	2016 DEC 19 20:40:19.1470	117581.59	117554.33	27.26	188.80
VIMS_alpOri277I	2017 JUN 04 22:40:28.7150	117598.39	117573.89	24.50	352.64

$$r_{\rm mod}(\lambda,t) = a + \sum_{i=1}^{M} \Delta r(m_i,\lambda,t). \tag{10}$$

Here, a is the semimajor axis of the B ring's outer edge and the summation is performed over the radial perturbations $\Delta r(m,\lambda,t)$ given by Eq. (3) associated with the M separate modes (*i.e.,* values of m) for a given ring model. The goodness of each fit is characterized by the reduced-χ^2 parameter

$$\chi^2 = \frac{1}{N-N_p}\sum_{i=1}^{N}[r_{\rm obs}(\lambda,t) - r_{\rm mod}(\lambda,t)]^2, \tag{11}$$

where N is the number of independent data points fitted and N_p is the number of parameters in the fit. This is usually expressed more intuitively in terms of the root-mean-square residual per degree of freedom (PDF), $\sigma = \sqrt{\chi^2}$.

We approach our search for possible normal modes by first fitting a circular model to the data, forming the residuals, and then scanning over a range of pattern speeds Ω_P in the vicinity of the predicted value for the mean radius, based on Eq. (2) and candidate wavenumbers from $m = 1$ to $m = 20$ for ILR-type perturbations. For each assumed value of m and Ω_P, we solve for the best-fitting amplitude A_m and phase δ_m and record the value of the RMS residual σ. We then add the strongest of the detected modes to the kinematical model of the B ring edge, form a new set of residuals, and repeat the frequency scanning process to search for additional modes. With the addition of successive normal modes, the post-fit value of σ is reduced and the sensitivity to weaker modes and possible libration terms is increased.

Once a preliminary set of global normal modes has been identified, we break the dataset into smaller segments and examine the observed variation in amplitude for each mode over the 13 yr time span of the observations. Based on these shorter-period fits, we solve for the characteristics of any necessary libration terms, as described by

Eq. (4) or (8), that can best account for the long-term trends seen in the mode amplitudes. In the next two sections, we turn to a description of the results of this process.

5. REFERENCE MODEL

Because the *Cassini* occultation data set has more than doubled in size from that used by Nicholson et al. (2014a) — 294 observations now vs 133 in the previous work — and also doubled in duration (over almost thirteen vs six years), our first step is to redo the best fit in Nicholson et al. (2014a) using all the currently-available *Cassini* occultation data. For this purpose, we compare our new results with those of Fit 11 in Nicholson et al. (2014a), as described in their Table 5. Note that both fits exclude the relatively small number of pre-*Cassini* observations, derived from *Voyager* and Earth-based occultations. Experiments show that while the longer time baseline provided by these earlier data improves the accuracy with which pattern speeds can be determined, the much sparser temporal coverage also leads to problems with aliasing and multiple solutions.

This fit, which we refer to henceforth as our reference model, includes — in descending order of importance — a circulating $m = 2$ mode, a free eccentricity (*i.e.*, an $m = 1$ mode), and fixed-amplitude normal modes with $m = 3$, 4 and 5. The $m = 2$ mode has two components: a forced eccentricity (which we denote as e_0) due to the Mimas 2:1 ILR and a free eccentricity (denoted as e_1) that we interpret as a normal mode.Departing slightly from Fit 11 in Nicholson et al. (2014a), where we fixed Ω_P for the forced $m = 2$ mode at the average value of Mimas's mean motion in 2005–2010 and fixed the corresponding phase δ_2 to be Mimas's mean longitude at our reference time, in the current fit we permit both parameters to float, with *a priori* values corresponding to the Mimas resonance. (Alternate fits in which Ω_P and δ_2 were fixed at their expected values were almost indistinguishable.) **Table 2** presents the results of this reference fit, which we will use below as a standard against which to compare our new fits that include additional librations.

A comparison with the parameters of Fit 11 of Nicholson et al. (2014a) reveals the following:

- The mean radius of the B ring edge is almost unchanged at $a = 117,570.32 \pm 0.42$ km. This is ∼14.5 km exterior to the nominal location of the Mimas 2:1 ILR at $a_{\rm res} = 117,555.8$ km (Spitale and Porco 2010).
- The minimum post-fit root-mean-square residual per degree of freedom is 6.98 km, comparable to but slightly lower than the 7.81 km obtained for Fit 11. This remains much larger than the typical measurement errors, which are well under 1 km for this sharp, well-defined edge, and also much larger than post-fit

Table 2. Reference model fit to *Cassini* data

Parameter	Symbol	Value
mean radius	a(km)	117570.32 ± 0.42
Forced $m = 2$ mode	ae_0(km)	33.20 ± 0.63
	Ω_P(° d^{-1})	381.9843 ± 0.0005
	δ_2(°)	346.83 ± 0.73
$m = 2$ libration	ae_1(km)	39.40 ± 0.64
	Ω_L(° d^{-1})	0.1841 ± 0.0008
	P_L (yr)	5.354 ± 0.023
	δ_L(°)	96.07 ± 1.86
Epoch	t_0	UTC 2008 Jan 1 12:00
RMS residual PDF	σ(km)	6.98
# data	N	294
Fit ID		ringfit_v1.8.Sa025S-CMF-V6980-RF-B95

m	A_m (km)	Ω_P (° d^{-1})	δ_m (°)
1	22.35 ± 0.59	5.0814 ± 0.0011	69.34 ± 2.14
3	9.54 ± 0.60	507.7185 ± 0.0008	24.48 ± 1.53
4	8.38 ± 0.58	570.5293 ± 0.0008	6.91 ± 1.43
5	5.87 ± 0.60	608.2073 ± 0.0008	67.98 ± 1.59

residuals obtained for most other sharp-edged features in the Cassini Division (French et al. 2016), suggesting that significant unmodeled radial perturbations remain.

- The larger component of the $m = 2$ mode is again the free (or normal) mode, whose amplitude has increased from 37.1 km to $ae_1 = 39.40 \pm 0.64$ km, while the forced component due to the Mimas resonance is almost unchanged at $ae_0 = 33.20 \pm 0.63$ km. The libration frequency remains almost unchanged at $\Omega_L = 0.1841 \pm 0.0008°$ d^{-1} with a corresponding period $P_L = 5.354 \pm 0.023$ yr [**I added this to the table -rgf**] , while the fitted pattern speed for the forced component is $\Omega_P = 381.9843 \pm 0.0005°$ d^{-1}, very close to the average mean motion of Mimas of 381.9835° d^{-1} during the period of the *Cassini* mission. [**Update this if necessary.**] Geometrically, this means that the angle ϕ_L circulates through 360° once every libration period ($= 2\pi/\Omega_L$) and that the minor axis of the $m = 2$ pattern rotates through 360° with respect to Mimas once every two libration periods, or ~ 10.7 yr (cf. Eq. (9)). (See Section 7.2 for further discussion of the significance of this point and of the phase lag of the forced component.)

- Next in importance is the $m = 1$ mode, or free eccentricity, which has increased somewhat in amplitude from 20.4 to 22.35 ± 0.59 km, but which has maintained its pattern speed almost unchanged at $5.0814 \pm 0.0011°$ d^{-1}.

- The $m = 3$ mode, on the other hand, has decreased in amplitude from 12.5 to 9.54 ± 0.60 km, while increasing its pattern speed by $\sim 6\sigma$ to $507.7185 \pm 0.0008°$ d^{-1}.
- Next is the $m = 4$ mode, which has increased significantly in amplitude from 5.9 to 8.38 ± 0.58 km, while increasing its pattern speed by $\sim 4\sigma$ to $570.5293 \pm 0.0008°$ d^{-1}.
- Lastly we have the $m = 5$ mode, which is almost unchanged in amplitude at 5.87 ± 0.60 km and in pattern speed at $608.2073 \pm 0.0008°$ d^{-1}.

To illustrate the reference model, **Figure 2** shows snapshots of the co-added modes over a period of two libration cycles, in the form of profiles of the radial displacement of the B ring edge as a function of longitude relative to Mimas. Note that the $m = 2$ mode has a maximum amplitude of ~ 72 km when its forced and free components are in phase but almost disappears when the two components are out of phase by π.

6. RESULTS

Having updated the mode fits of Nicholson et al. (2014a) with the more complete *Cassini* data set, we turn to our major task, which is to characterize the decadal-scale variations in the identified normal modes, if any, and to search for additional perturbations that may have escaped detection in previous analyses of the B ring edge.

For each mode, we scan a range of pattern speeds for the specified value of m in the neighborhood of the expected rate, as given by Eq. (2), in order to verify the reality of the mode and search for evidence of additional, nearby modes. Each scan is constructed in the same fashion: (i) the fit parameters for all m-values not being scanned are frozen at their best-fit values in Table 2; (ii) the fit parameters for the mode in question other than the pattern speed Ω_P are allowed to float; (iii) the value of Ω_P is varied across a range of $\pm 1°$ d^{-1} centered on the predicted rate at the edge of the B ring, and (iv) for each assumed value of Ω_P the remaining mode parameters A_m and δ_m are adjusted to minimize the value of χ^2. In this way, the significance of each mode can be assessed, with the parameters of all other modes kept constant at their optimal values.

The rms residuals far away from the best-fitting value of Ω_P reflect the quality of the fit without the mode in question; for the dominant $m = 2$ mode this is ~ 34 km. For the weaker $m = 3$, 4 and 5 modes, the baseline rms residuals are always under 10 km.

We begin with the dominant $m = 2$ mode and then move on to the smaller-amplitude modes with $m = 1$, 3, 4 and 5.

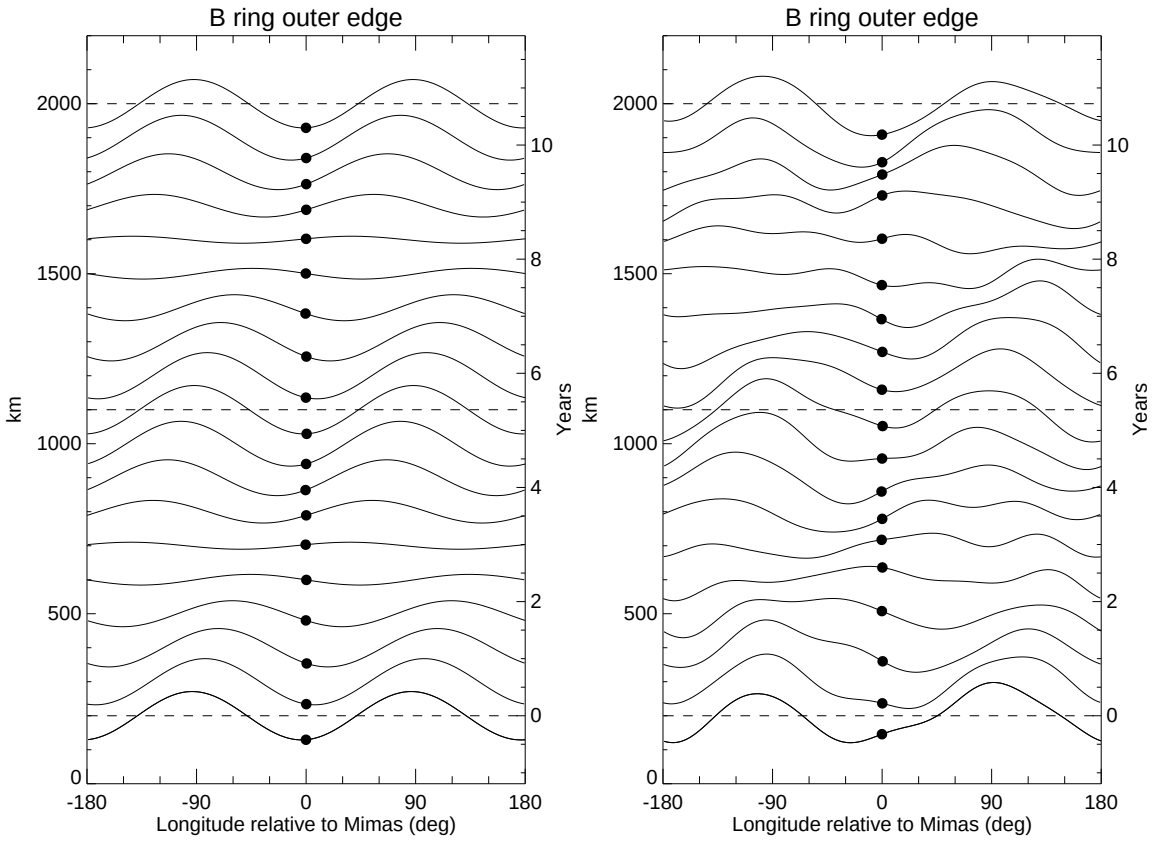

Figure 2. Representative profiles of the B ring edge over two libration periods, plotted in radius (on the left axis) and time (on the right axis) as a function of longitude relative to Mimas, whose position is indicated by the large filled circles. The left panel shows the $m = 2$ mode only, while the right panel includes all five modes. The bottom profiles correspond to a time when the forced and free components of the $m = 2$ mode are in phase (*i.e.,* $\phi_L = 0$), so that the amplitude of the mode is at its maximum value. Successive profiles are at intervals of 1/9 of the $m = 2$ libration period, and offset upwards by 100 km for clarity. Horizontal dashed lines mark successive $m = 2$ libration periods of 5.354 yr.

6.1. *Mimas and the dominant m=2 pattern*

For the $m = 2$ scan, both the forced and free amplitudes ae_0 and ae_1 were set to zero and the scanning program searched for a single, best-fitting mode. **Figure 3** shows the resulting scan. The predicted pattern speed for a free normal mode at the edge of the B ring is 381.913° d^{-1}, as indicated by the vertical solid line, while the pattern speed for the forced Mimas 2:1 perturbation is at $n_{\rm Mimas} = 381.9835°$ d^{-1}, indicated by the dot-dashed line. As might be expected from the reference fit parameters in Table 2, the scan shows two distinct peaks in amplitude in the lower panel — and two corresponding minima in the post-fit residuals in the upper panel — at $\sim 381.984°$ d^{-1} and 382.075° d^{-1}. The higher and faster peak corresponds to the free $m = 2$ mode while the lower and slower peak corresponds to the forced mode. The fitted libration frequency in Table 2 of $\Omega_L = 0.1841°$ d^{-1} is twice the difference between the two mode peaks, as expected from Eq. (7). Note that, because the scanning procedure is only

able to fit one pattern speed at a time, the minimum rms residual seen in Fig. 3 is still quite large at ∼24 km. Finally, we note that the resonance radius[4] corresponding to the free mode is located at ∼117,537 km, or 33 km interior to the mean radius of the B ring edge.

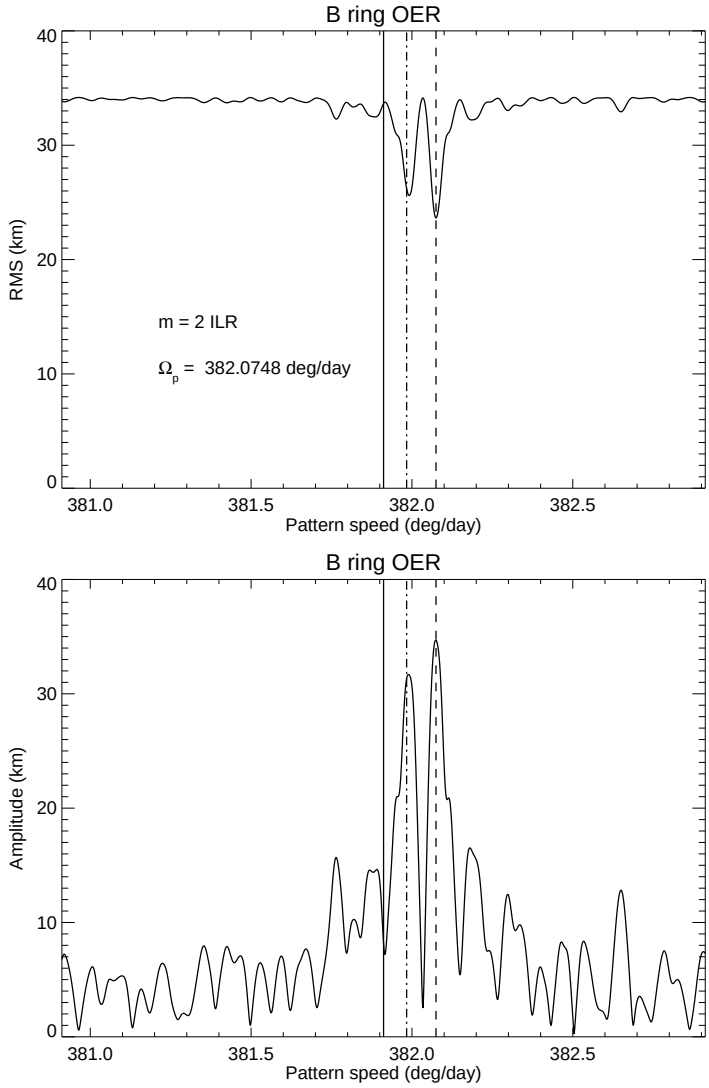

Figure 3. A scan in pattern speed for $m = 2$ normal modes, after removing the signatures of all other modes listed in Table 2. The upper panel shows the root-mean-square residual of the fit σ as the pattern speed is scanned across the expected value, while the lower panel shows the fitted radial amplitude of the mode A_2 for the same scan. Note the detection of significant power at two different pattern speeds, 381.984° d^{-1} and 382.075° d^{-1}, with radial amplitudes of 31 and 36 km. The solid vertical line indicates the predicted value of Ω_P at the mean radius of the B ring's outer edge, or 381.913° d^{-1}, while the dashed line highlights the value of Ω_P for the strongest peak in the scan, with a minimum $\sigma = 23.9$ km. The dot-dashed line indicates the average mean motion of Mimas of 381.9835° d^{-1}.

[4] That is, the semimajor axis at which Eq. (2) is satisfied.

The existence of these two $m = 2$ components of comparable strength results in a strong beat signature that can also be modeled as a circulation in the amplitude and phase of a single $m = 2$ mode, with parameters as listed in Table 2. As a result, the amplitude of the $m = 2$ pattern varies significantly during the *Cassini* mission, as first noted by Hedman et al. (2010) and Spitale and Porco (2010). This amplitude variation is clearly revealed in **Fig. 4**, which shows fits to subsets of the occultation data in eight different time intervals, selected to match the most densely-sampled periods. For each period, the radius residuals are calculated relative to our adopted reference model — except that the amplitudes of the $m = 2$ terms, ae_0 and ae_1 are set to zero — and plotted vs the mode argument $m\theta = m[\lambda - \Omega_P(t - t_0) - \delta_m]$ in Eq. (1), where in this case $m = 2$. In this figure, and in the similar ones to follow for other values of m, the upper left panel shows the complete set of *Cassini* observations, while the eight successive panels reveal any systematic changes in both the amplitude and the phase of the $m = 2$ pattern over time.

Because the argument $m\theta$ includes the best-fitting global pattern speed and average phase for the mode, as represented by the parameters Ω_P and δ_m in Eq. (1), any shorter-term variations in the mode's phase will show up here as shifts in the position of the minimum in radius away from $m\theta = 0$ from one time period to another. Indeed, such variations are clearly seen in this figure, with the radial minimum varying from $m\theta = -86°$ in 2006/07 to $+120°$ in 2017. Moreover, the amplitude varies from a minimum of ∼6 km in 2017 to a maximum of ∼70 km in 2009. In order to quantify these variations for the time period of the data shown in each panel, we fit a simple sinusoidal model to the distribution of radius residuals of the form:

$$dr = -ae\cos(m\theta - \phi_L), \tag{12}$$

following Eq. (3). The fitted values (and their formal uncertainties) for ae and ϕ_L are listed in each panel.

These fitted variations in the amplitude of the $m = 2$ mode are compared with those predicted by the circulating model in the reference fit in **Fig. 5**, where the colored symbols mark the times of the individual observations (blue for stellar occultations and red for RSS measurements). The eight large '+' symbols mark the fitted values for ae from Fig. 4, with the vertical component showing the formal uncertainty in the amplitude fit and the horizontal length spanning the time interval of the data used for the fit. The second and eighth intervals span the minima in A_2 in 2006 and 2017, while the fourth interval spans the maximum in 2009. The observations sample a little over 2.5 libration cycles, or more than one rotation of the $m = 2$ pattern relative to Mimas, albeit with several gaps owing to the absence of ring occultation measurements when *Cassini* was orbiting Saturn in the equatorial plane. Note that the amplitude lingers near its maximum value of 72.6 km for about a year, while moving rapidly through its minimum of 6.2 km in only a few months, making it difficult to catch the system in

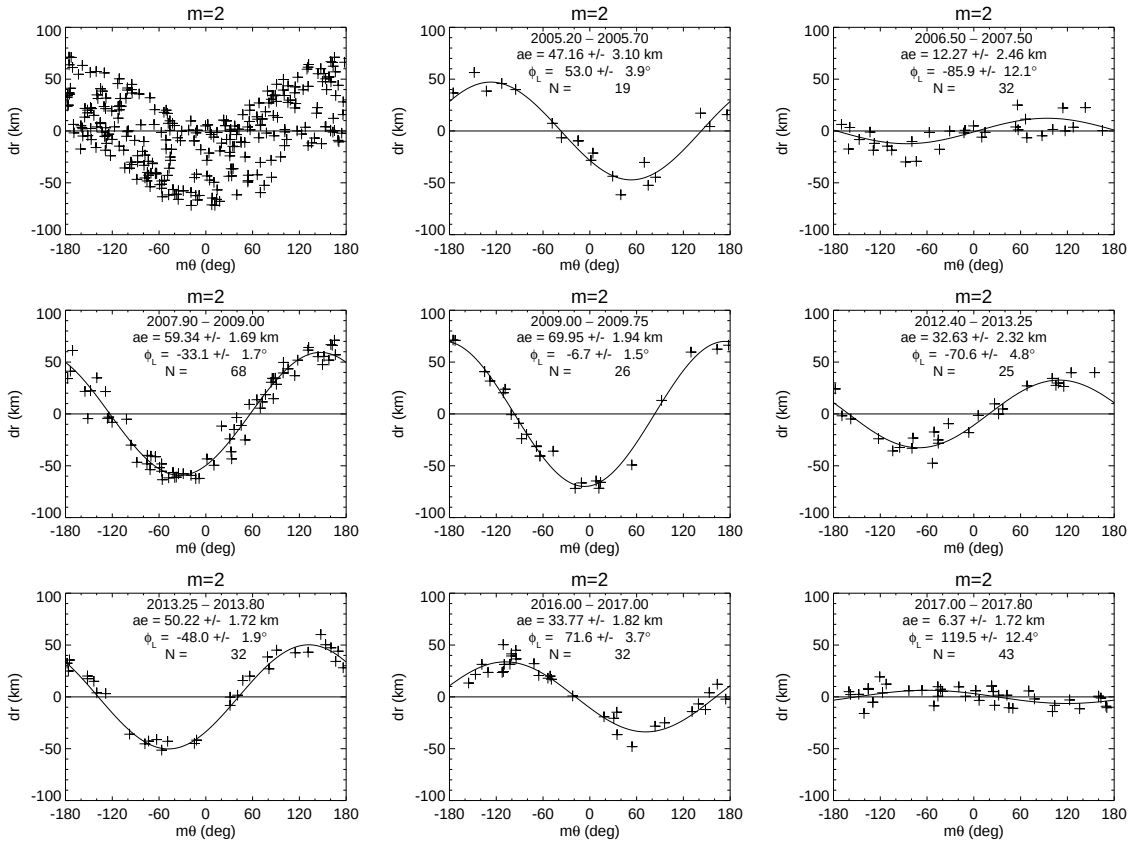

Figure 4. Radius residuals from our reference model when the free and forced $m = 2$ terms are set to zero, plotted as a function of $m\theta$. The upper left panel shows the full set of observations, with substantial scatter. The observations are divided into eight different time intervals in the remaining panels, showing substantial systematic variations in the amplitude and phase of the $m = 2$ pattern over time. See text for details of the model fit results included in these panels.

this state. In general, the agreement between the reference model and these individual fits over the eight separate time ranges is excellent. (Very similar results are obtained when the $m = 2$ amplitude ae is computed using our adopted final fit.)

Because $ae_1 > ae_0$ for the $m = 2$ mode, there is a substantial variation in the phase of this mode compared to that predicted by Eq. (1). In fact, our model implies that ϕ_L actually circulates through 360°, as concluded originally by Spitale and Porco (2010), although the system spends relatively little time with $|\phi_L| > 90°$. This may be seen in **Fig. 6**, which shows the distribution of the B ring edge measurements used in this study along with the corresponding phases predicted by the reference model ϕ_L. We find that $|\phi_L| > 90°$ for about 9 months every 5.4 years, centered on the times of the amplitude minima in 2006.7, 2012.1 and 2017.5. (Amplitude maxima occur in 2009.4 and 2014.8, when ϕ_L passes through zero.)

Updated values for the $m = 2$ libration parameters are included in our final fit that includes all known modes and librations (see **Table 3** below). Following a similar

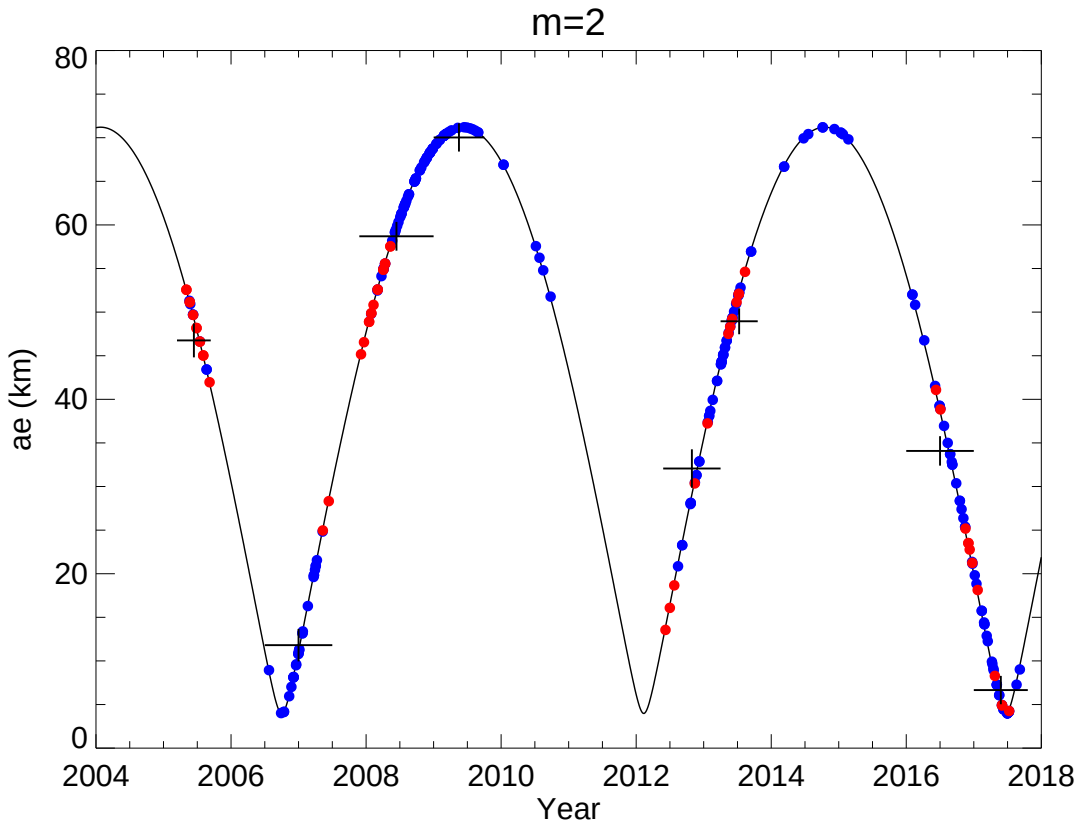

Figure 5. The variation in the $m = 2$ amplitude ae, as computed from the reference model. Blue dots mark the times of individual stellar occultation observations, and the red symbols mark RSS observations. Fitted average values over the eight selected intervals in Fig. 4 are shown as large '+' symbols, with the vertical extent showing the formal uncertainty in the amplitude and the horizontal extent representing the time span of data used in each fit.

process to that used for the other wavenumbers (described below), we also scanned the residuals to this final fit to search for any additional, previously-undetected contributions to the $m = 2$ pattern, but found none.

6.2. *The m=1 pattern*

Figure 7 shows the pattern speed scan for the $m = 1$ mode, whose predicted value at the edge of the B ring is $\dot{\varpi}_{\rm sec} = 5.059°$ d^{-1}, as indicated by the vertical solid line. Here we see a single strong peak in amplitude at $\Omega_p = 5.083°$ d^{-1}, somewhat faster than the predicted value. The corresponding resonance radius is ∼117,419 km, or 151 km interior to the mean radius of the ring edge.

The reference fit for the $m = 1$ mode assumes a constant amplitude over the entire set of observations, but Nicholson et al. (2014a) noted that A_1 decreased slightly from ∼25 km in 2005 to ∼20 km in 2008/09 (see their Fig. 4). By separating the observations into the same eight time intervals as for the $m = 2$ mode, we see a more complete picture of the time variability of the $m = 1$ mode in **Fig. 8**. (In this and in subsequent

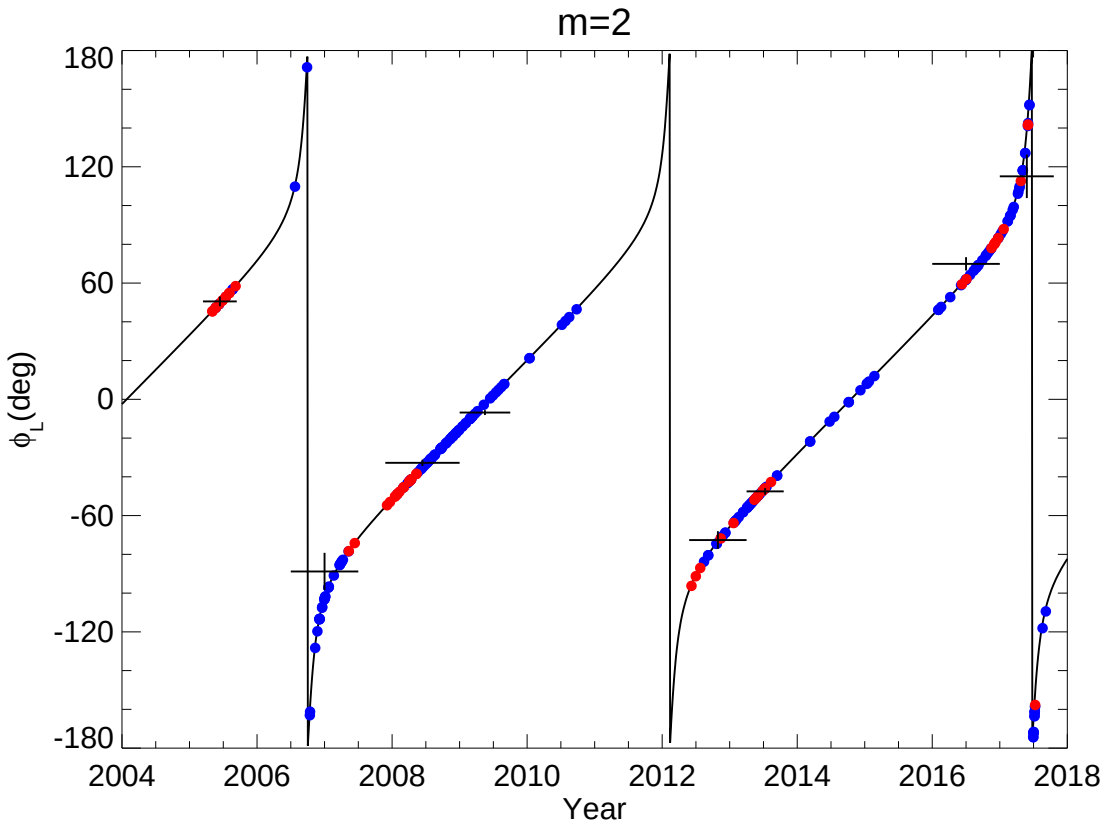

Figure 6. The variation in the $m = 2$ libration phase ϕ_L, as computed from the reference model. Note the highly non-uniform rate $d\phi_L/dt$ as the time-varying eccentricity vector sweeps rapidly through its minimum range. As in Fig. 5, blue symbols mark the times of stellar occultation observations and red symbols mark RSS observations. The fitted average phase values over the eight selected intervals in Fig. 4 are shown as large '+' symbols, with the vertical extent showing the formal uncertainty in the average phase over the interval and the horizontal extent representing the time span of data used in each fit.

similar figures, we compute the residuals relative to our final adopted model for the B ring, rather than to the reference model, since this more realistically shows the radial variations that contribute to the final fit for each wavenumber.) With a doubling of the timespan of the observations, we confirm the results of Nicholson et al. (2014a) but find that A_1 subsequently increased to ∼30 km in 2013, before falling back to ∼17 km in 2016/17.

Given this evidence for time variability in the $m = 1$ amplitude, we repeated our frequency scan of the B ring edge residuals after removal of the main $m = 1$ signal, as well as all other detected normal modes from our final fit (see Table 3 below), with the results shown in **Fig. 9**. We find a much weaker but statistically-significant signal with $\Omega_P = 5.206°$ d^{-1} and an amplitude of 4.4 km. Combined with the original $m = 1$ mode with $\Omega_P = 5.083°$ d^{-1}, this suggests a libration with $\Omega_L \simeq 0.123°$ d^{-1}, corresponding to a period of ∼ 8.0 yr.

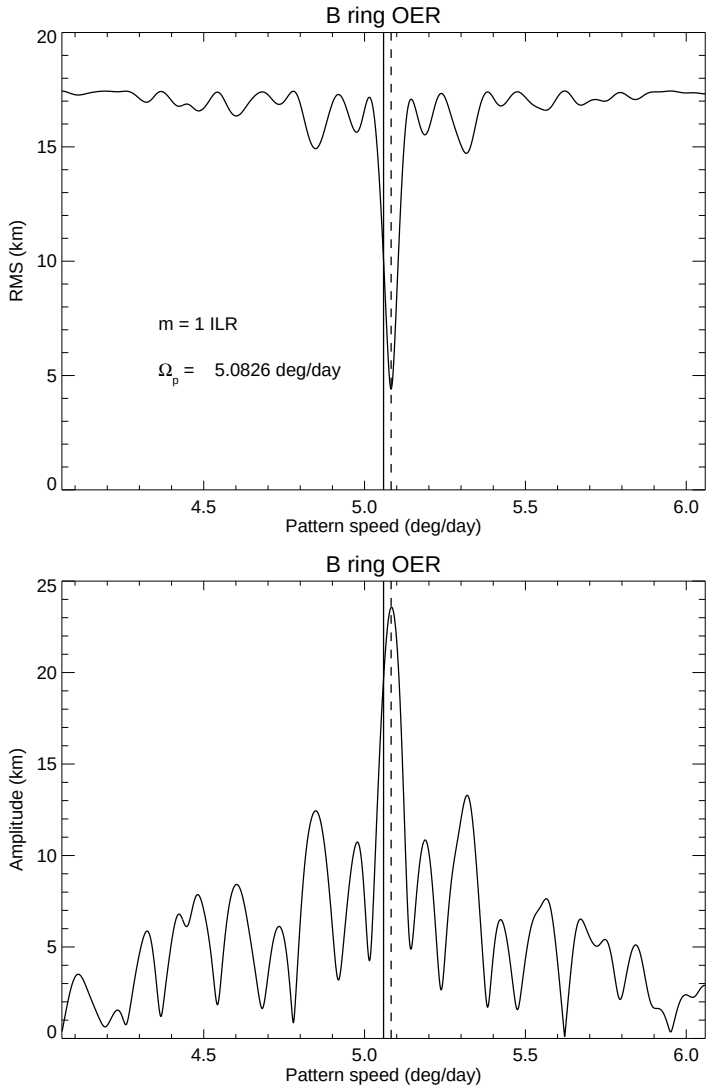

Figure 7. A scan in pattern speed for $m = 1$ normal modes, after removing the signatures of all other modes listed in Table 2. The format is the same as Fig. 3. Here significant power is seen at only one frequency, at 5.083° d^{-1}, with a radial amplitude of 23.6 km and a minimum $\sigma = 4.4$ km.

Although including this libration term in the $m = 1$ mode does modestly improve the overall fit, it fails to capture well the amplitude variations seen in Fig. 8. A subsequent frequency scan, after inclusion of the above libration term, shows evidence for a third statistically-significant $m = 1$ component with $\Omega_P = 5.250°$ d^{-1} and an amplitude of ~ 2.8 km, as shown in **Fig. 10**. This suggests a second libration term with $\Omega_L \simeq 0.167°$ d^{-1}, corresponding to a period of ~ 5.9 yr.

Once this additional component is included in the orbit fit, the calculated amplitude and phase variations of the $m = 1$ mode provide a significantly better match to the observations, as shown in **Fig. 11**. We caution the reader, however, that while this multi-component model may match our observations over their 13 yr time interval,

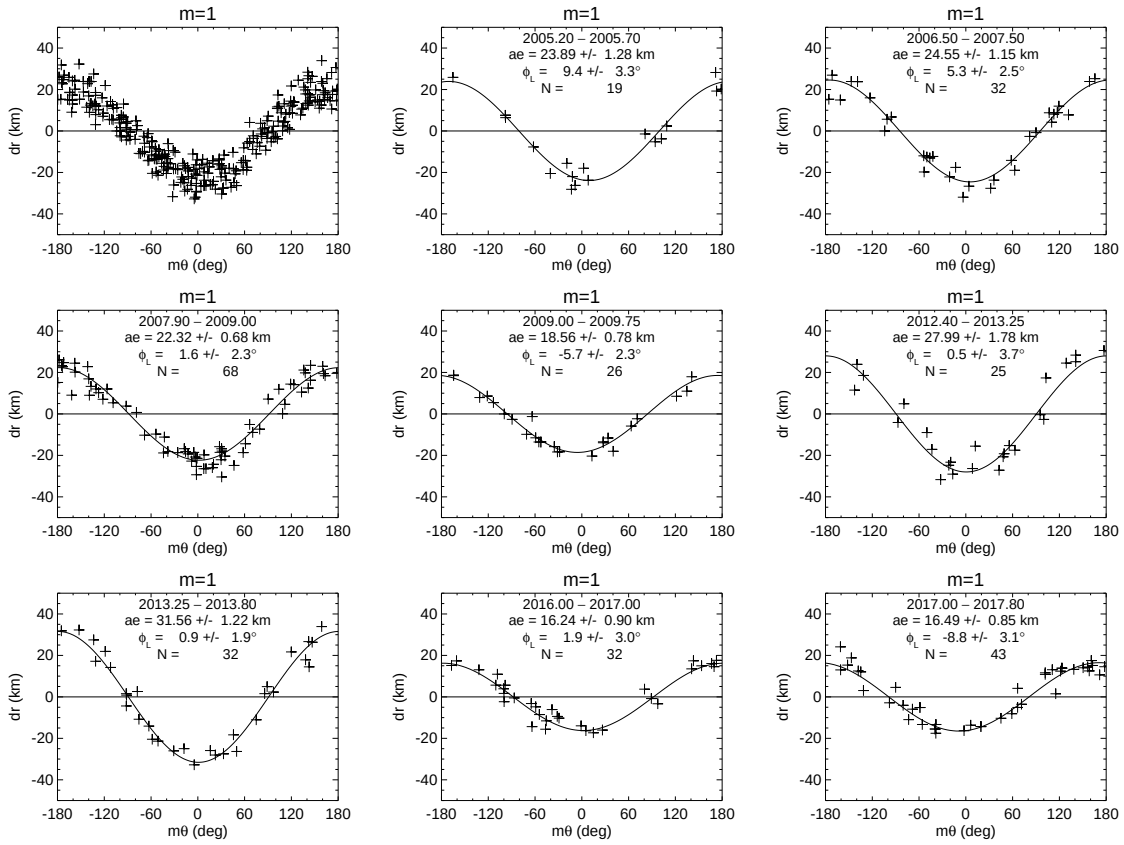

Figure 8. Radius residuals from our final B ring model when the $m = 1$ terms are set to zero, plotted as a function of $m\theta$. The upper left panel shows the full set of observations, with substantial scatter. The observations are divided into eight different time intervals in the remaining panels, as in Fig. 4, showing substantial systematic variations in the amplitude of the $m = 1$ pattern over time, particularly after 2010. See text for details of the model fit results included in these panels.

we do not know if these librations will maintain their amplitudes, periods, and phases over timescales of centuries. Instead, it might be better to think of them simply as quantifying the variability of the $m = 1$ shape of the B ring edge over the limited period of *Cassini* observations.

Table 3 includes the final values for all three $m = 1$ components in our adopted fit, with amplitudes of $ae_0 = 23.56 \pm 0.51$ km, $ae_1 = 4.42 \pm 0.63$ km, and $ae_2 = 2.84 \pm 0.53$ km. The final libration frequencies are $\Omega_{L,1} = 0.1145 \pm 0.0096°$ d^{-1} and $\Omega_{L,2} = 0.1671 \pm 0.0150°$ d^{-1}.

6.3. *The m=3 pattern*

Figure 12 shows the scan for the $m = 3$ mode, whose predicted pattern speed at the edge of the B ring is $\Omega_P = 507.530°$ d^{-1}. Here we see a single strong peak in amplitude at $\Omega_p = 507.7189°$ d^{-1}, again faster than the predicted value, but also two secondary peaks at slightly lower frequencies. The resonance radius corresponding to

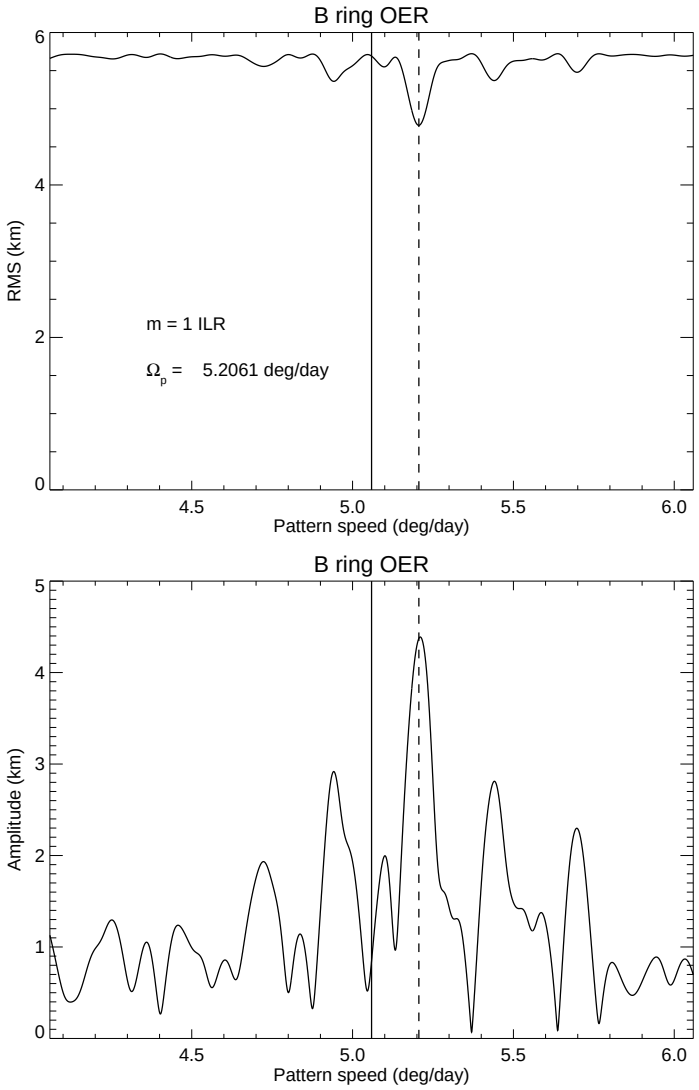

Figure 9. The signature of a second $m = 1$ component with $\Omega_P = 5.206°$ d^{-1} and an amplitude of $\sim$ 4.4 km, as seen in a normal mode scan. The primary component is at $\Omega_P = 5.083°$ d^{-1}, as shown in Fig. 7, while the predicted pattern speed at the edge of the B ring is $5.059°$ d^{-1}.

the strongest peak is ∼117,541 km, or 29 km interior to the mean radius of the ring edge.

As for the $m = 1$ mode, we again find substantial long-term variations in the amplitude and phase over time, as shown in **Fig. 13**, which follows the same format as Figs. 4 and 8. Beginning at $\sim$ 20 km in 2005, ae fell steadily to a minimum of $\sim$ 7 km in 2009-2013, rose to 11 km in 2016, before falling slightly in 2017. The steady decline between 2005 and 2009 was also noted by Nicholson et al. (2014a).

In our initial attempt to match this pattern, we included a single libration term for $m = 3$, treating the libration frequency Ω_L, amplitude ae_1, and phase δ_L as free parameters. The results matched the overall trend in the amplitude of the mode, but

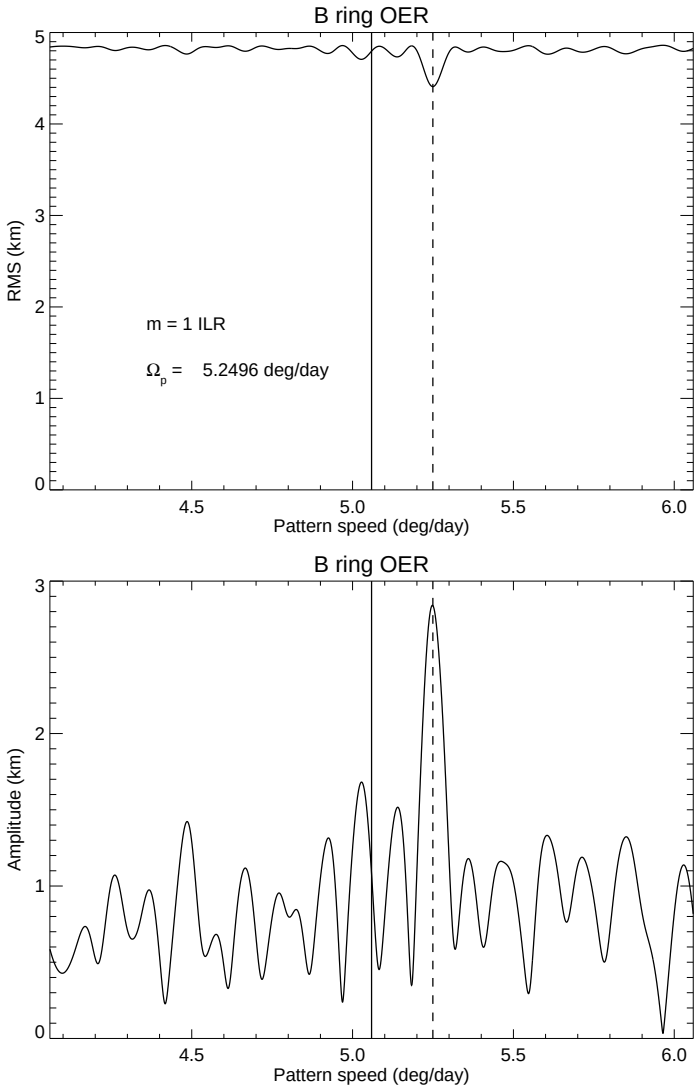

Figure 10. The signature of a third $m = 1$ component with $\Omega_P = 5.250°$ d^{-1} and amplitude ~ 2.8 km. The primary and secondary components are at $\Omega_P = 5.083°$ d^{-1} and $5.206°$ d^{-1}, as shown in Figs. 7 and 9.

with physically implausible values for ae_0 and ae_1 of hundreds of km and a libration period of hundreds of years, much longer than those found for the $m = 1$ and $m = 2$ modes. The two components nearly cancel each other out during the comparatively short interval of the *Cassini* observations, but lead to much larger — and implausible — predicted variations at earlier and later times.

As with the $m = 1$ case, we then fitted for a second libration component with much more satisfactory results, as shown in **Fig. 14**. The dominant component, however, has an uncomfortably long period of almost 20 yrs — longer than the 13 yr span of the *Cassini* observations — that is not well-determined by the fit. Table 3 includes the final values for all three $m = 3$ components in our adopted fit, with amplitudes of $ae_0 = 11.19 \pm 0.53$ km, $ae_1 = 7.41 \pm 0.64$ km, and $ae_2 = 2.15 \pm 0.49$ km. The

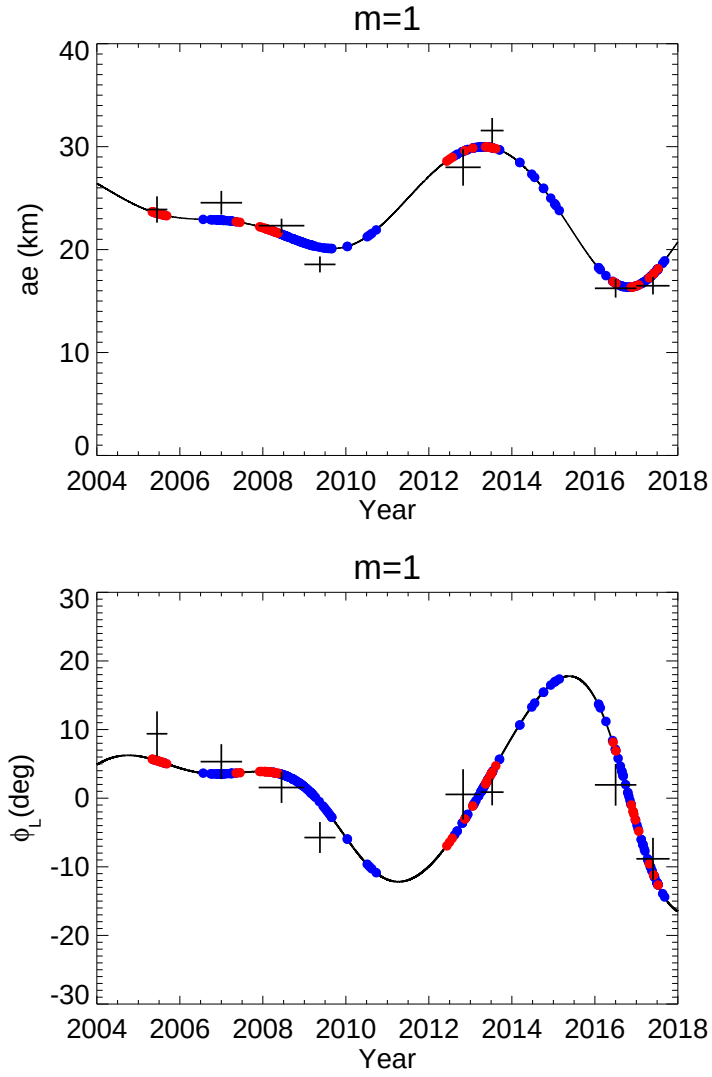

Figure 11. Variation in the amplitude A_1 and phase ϕ_L of the $m = 1$ mode over time incorporating two libration terms with periods of 8.0 and 5.9 yr and amplitudes of 4.4 and 2.8 km, respectively. The model curves matches the fitted values for the mode amplitude and libration phase obtained from fits to selected time intervals shown in Fig. 8 over the full span of the observations, although extending these periodic terms into the unobserved past or future is probably unwarranted.

final libration frequencies are the poorly-constrained value of $\Omega_{L,1} = -0.050°$ d^{-1} and $\Omega_{L,2} = 0.1342 \pm 0.0086°$ d^{-1}. (Note that a negative value of Ω_L implies that the eccentricity vector rotates in a clockwise direction in $[h, k]$ space and that, if the libration is interpreted in terms of the beating of two modes with the same m, that $\Omega_1 < \Omega_0$ in Eq. (7)).

6.4. *The m=4 pattern*

Figure 15 shows the scan for the $m = 4$ mode, for which the predicted pattern speed at the edge of the B ring is $\Omega_P = 570.339°$ d^{-1}. Again we see a single strong

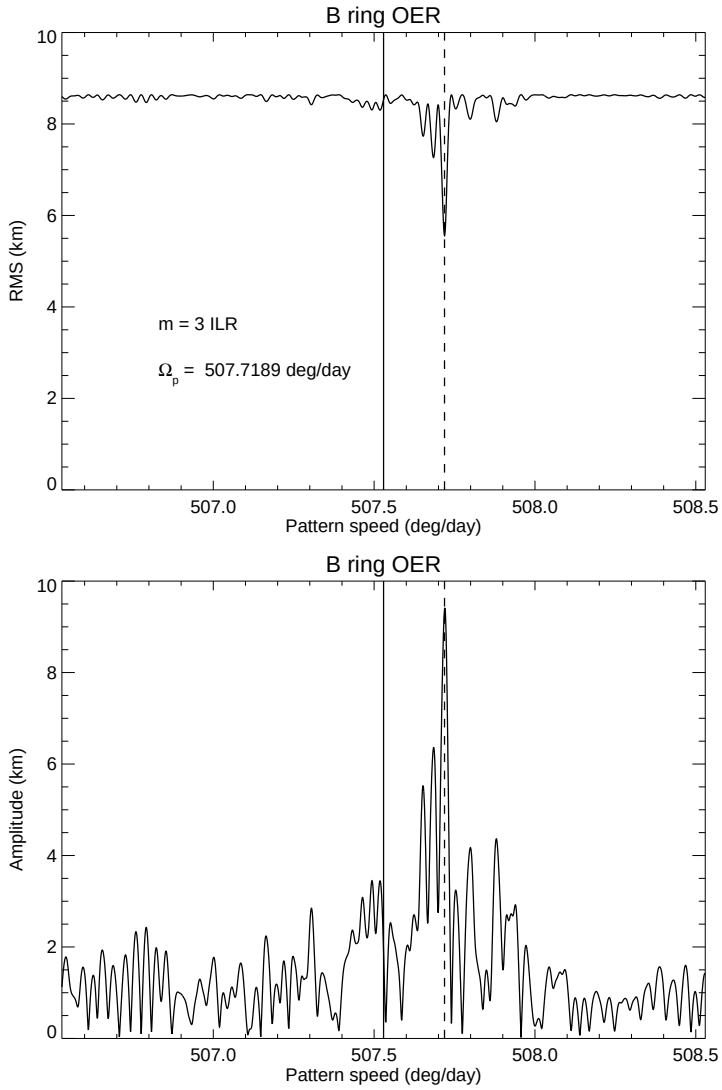

Figure 12. A scan in pattern speed for $m = 3$ normal modes, after removing the signatures of all other modes listed in Table 2. The format is the same as Fig. 3. Here the maximum power is seen at one frequency, at 507.7189° d^{-1}, with a radial amplitude of 9.5 km and a minimum σ = 5.6 km, but there are two substantial secondary peaks at slightly lower frequencies.

peak in amplitude at a pattern speed slightly faster than the predicted value, or $\Omega_p = 570.529°\ d^{-1}$. The corresponding resonance radius is ∼117,544 km, or 26 km interior to the mean radius of the ring edge.

The observed variations in the $m = 4$ contribution to the shape of the B ring edge over time are shown in **Fig. 16**, in the same format as Figs. 4, 8 and 13. As is the case for $m = 1$ and $m = 3$, we see substantial changes in amplitude over the course of the observations. Although the average amplitude is ∼8 km over the period 2005–2017 (see Table 2), it reached a minimum of ∼ 2.9 km in 2009 and a maximum of ∼ 14 km in 2017, without any clear periodicity.

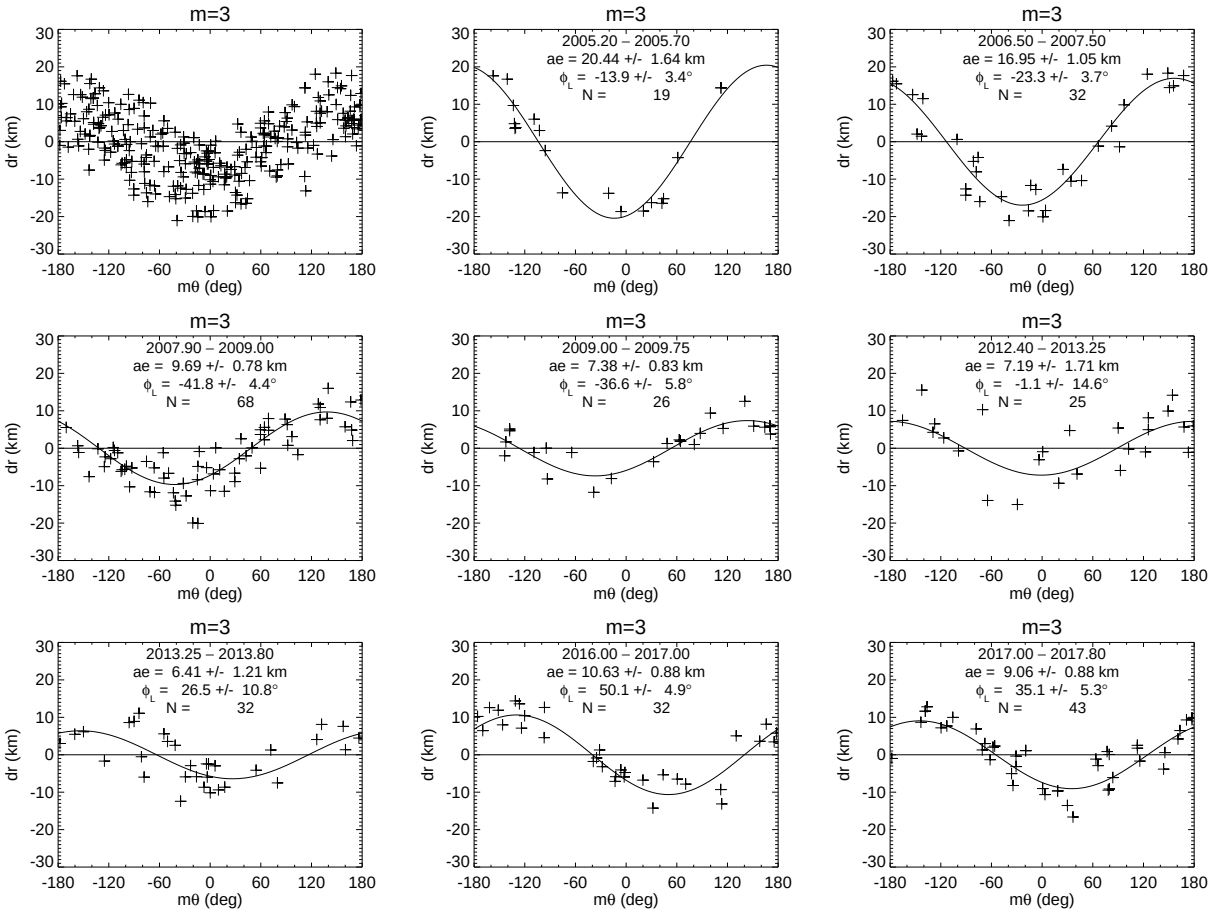

Figure 13. Radius residuals from our final B ring model when the $m = 3$ terms are set to zero, plotted as a function of $m\theta$. The upper left panel shows the full set of observations, with their substantial scatter. The observations are divided into eight different time intervals in the remaining panels, which show substantial systematic variations in the amplitude and phase of the $m = 3$ pattern over time. The amplitude decreased sharply between 2005 and 2010, remained fairly constant through 2013 and rose again in 2016 and 2017, though remaining well below the level of the earliest observations. See text for details of the model fit results included in these panels.

A libration frequency scan suggested a dominant frequency $\Omega_L \simeq 0.17^\circ$ d^{-1}, corresponding to a period of ~ 5.8 yr, with an amplitude of ~ 3 km, but a fit with such a single term was again rather unsatisfactory. A subsequent frequency scan of the radius residuals after inclusion of the single libration revealed a statistically significant additional component. A greatly improved fit to the observed amplitudes and phases was obtained with the resulting two-term libration model, as shown in **Fig. 17**. Table 3 includes the final values for all three $m = 4$ components in our adopted fit, with amplitudes of $ae_0 = 7.32 \pm 0.47$ km, $ae_1 = 2.79 \pm 0.47$ km, and $ae_2 = 2.56 \pm 0.45$ km. The final libration frequencies are $\Omega_{L,1} = -0.2032 \pm 0.0092^\circ$ d^{-1} and $\Omega_{L,2} = 0.1676 \pm 0.0095^\circ$ d^{-1}.

6.5. *The m=5 pattern*

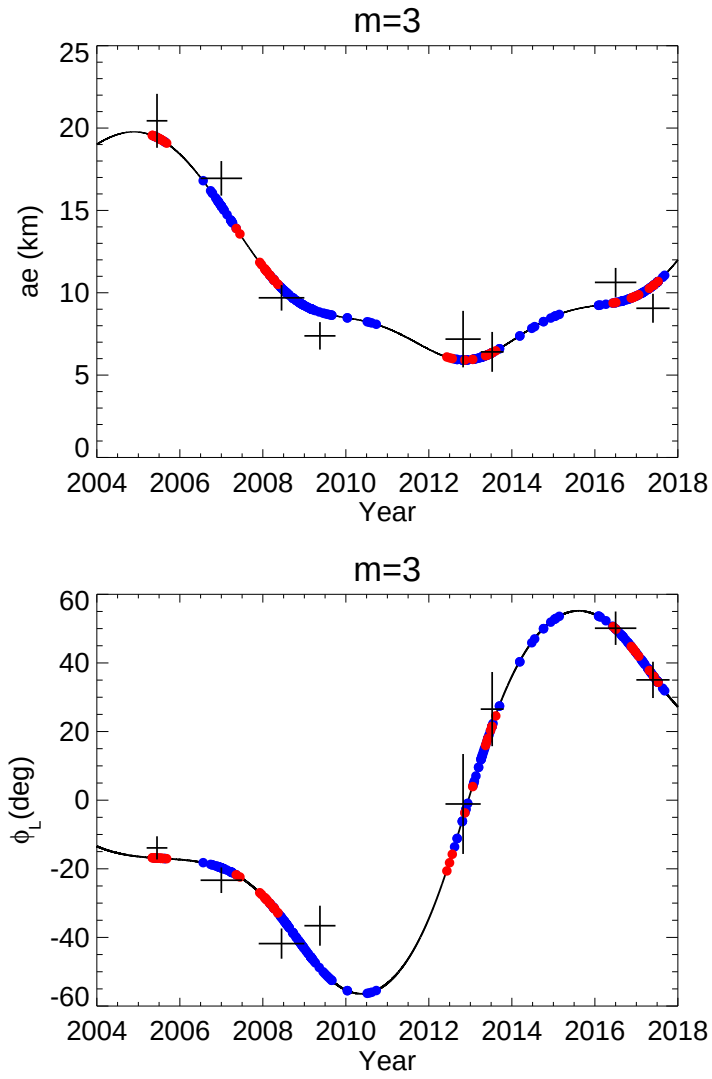

Figure 14. Variation in the amplitude A_3 and phase ϕ_L of the $m = 3$ mode over time incorporating two libration terms with periods of 19.7 and 7.3 yr and amplitudes of 7.4 and 2.2 km, respectively. The model curves match the fitted values for the mode amplitude and libration phase obtained from fits to selected time intervals shown in Fig. 13 over the full span of the observations, although the unusually long period of the first libration is not tightly constrained by the observations.

Finally we have **Fig. 18**, which shows the scan for the $m = 5$ mode, whose predicted pattern speed at the edge of the B ring is $\Omega_P = 608.025°$ d^{-1}. Again we see a single strong peak in amplitude at $\Omega_p = 608.206°$ d^{-1}, slightly faster than the predicted value. The corresponding resonance radius is ∼117,547 km, or 23 km interior to the mean radius of the ring edge. This is a relatively weak mode, with an average amplitude of about 6 km, but varying between about 4 and 8 km, as shown in **Fig. 19**. There appear to be at least three amplitude minima within the period of *Cassini* observations, in 2005, 2008 and 2016/17, suggesting a fairly short libration period.

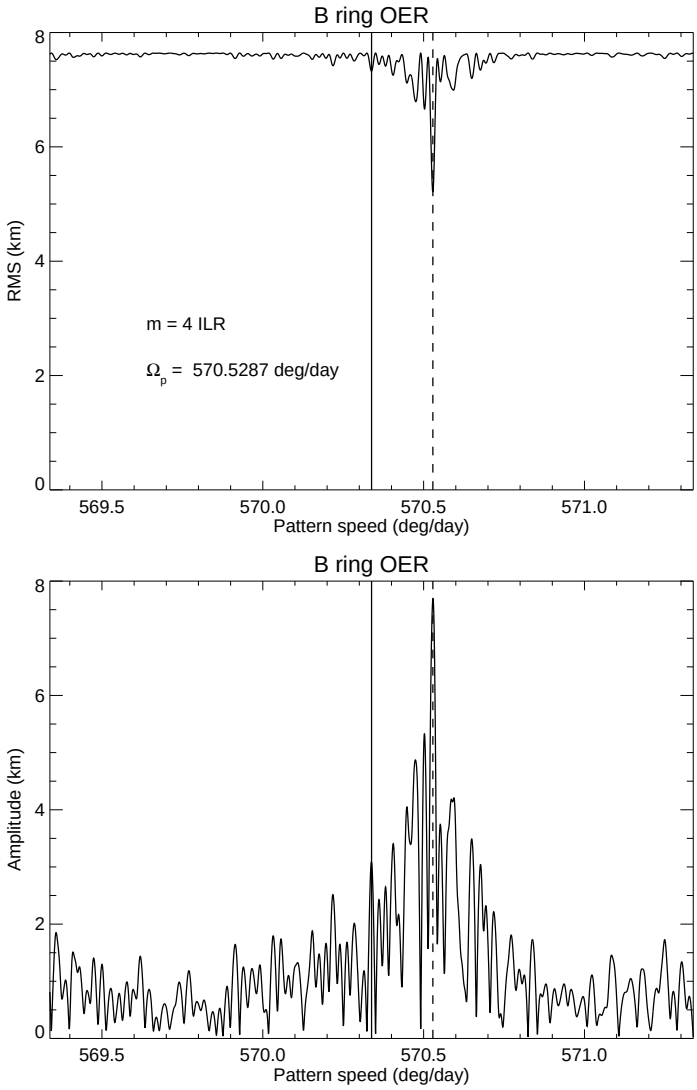

Figure 15. A scan in pattern speed for $m = 4$ normal modes, after removing the signatures of all other modes listed in Table 2. The format is the same as Fig. 3. Here the maximum power is seen at one frequency, at 570.529° d^{-1}, with a radial amplitude of 7.7 km and a minimum $\sigma = 5.2$ km.

A libration frequency scan revealed a single best-fitting value of $\Omega_L \simeq 0.44°$ d^{-1}, corresponding to a period of 2.25 yr, a result that was borne out by a least-squares fit with a single libration term. **Fig. 20** shows the resulting model amplitude and phase variations over time. Although the relatively rapid libration is less well-sampled by the eight snapshots in Fig. 19 than one would like, the model does fit the observations quite well. Our final model in Table 3 has $m = 5$ amplitudes of $ae_0 = 5.42 \pm 0.44$ km and $ae_1 = 1.55 \pm 0.44$ km, with a libration frequency $\Omega_L = 0.4353 \pm 0.0116°$ d^{-1}.

6.6. *Summary of libration models*

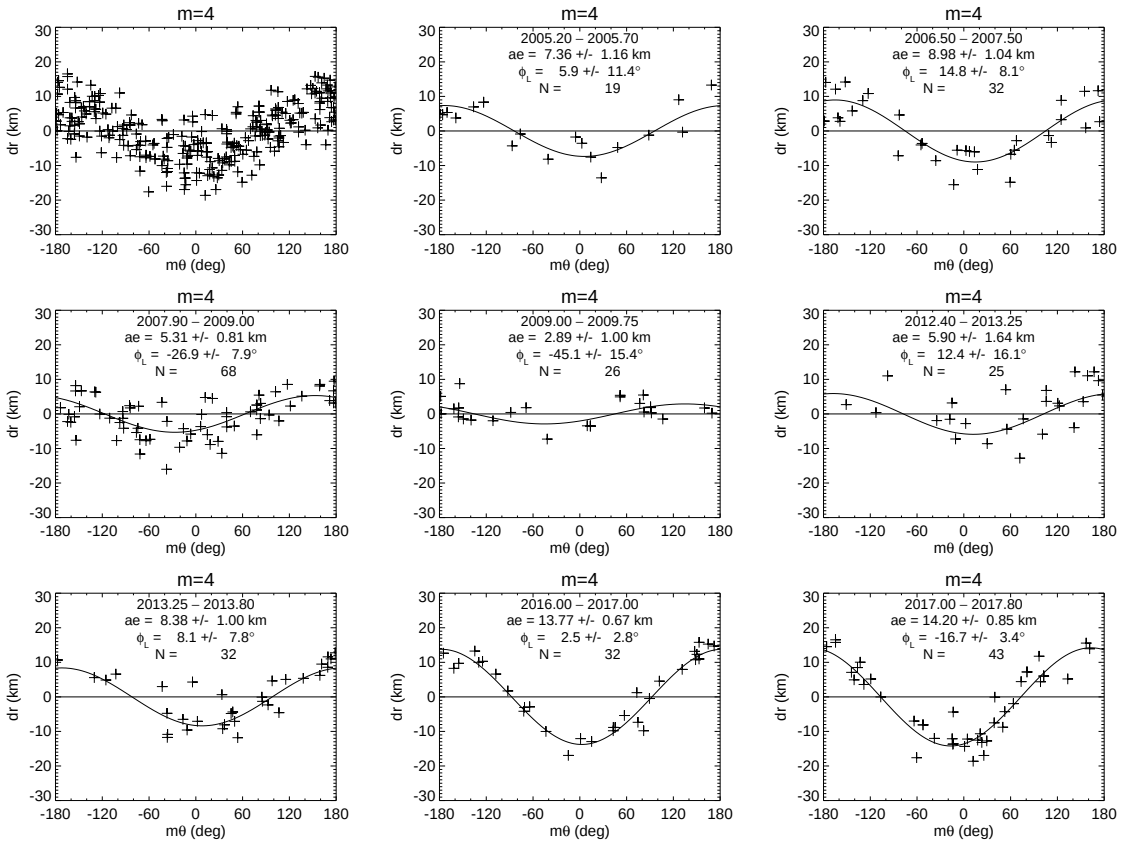

Figure 16. Radius residuals from our final B ring model when the $m = 4$ terms are set to zero, plotted as a function of $m\theta$. The upper left panel shows the full set of observations, with their scatter. The observations are divided into eight different time intervals in the remaining panels, which show substantial variations in the amplitude and phase of the $m = 4$ pattern over time, with the amplitude decreasing to below 3 km in 2009 and then rising to above 14 km in 2017. See text for details of the model fit results included in these panels.

Table 3 summarizes all the parameters for our final multi-mode fit to the B ring edge, including the libration terms. For each value of m we list the basic mode parameters ae_0, Ω_P and δ_m, and for each libration we list ae_j, $\Omega_{L,j}$ and $\delta_{L,j}$, as well as the libration period $P_{L,j}$. (Recall that for librating modes the overall amplitude $A_m = ae$ is not constant, but given by Eqns. (5) and (4) or (8).)

The rms residual per degree of freedom of the fit is 4.7 km, a significant improvement over the 7.0 km in the reference fit in Table 2 and the 7.8 km achieved by Fit 11 of Nicholson et al. (2014a). This improvement primarily reflects the addition of libration terms for the modes with $m = 1$, 3, 4 and 5. **Fig. 21** shows a histogram of the post-fit residuals in radius, compared to a Gaussian distribution with a standard deviation of 4.7 km. The 11 points with residuals > 20 km (*i.e.*, $> 4\sigma$) are listed in Table 1 and were excluded from the fit.

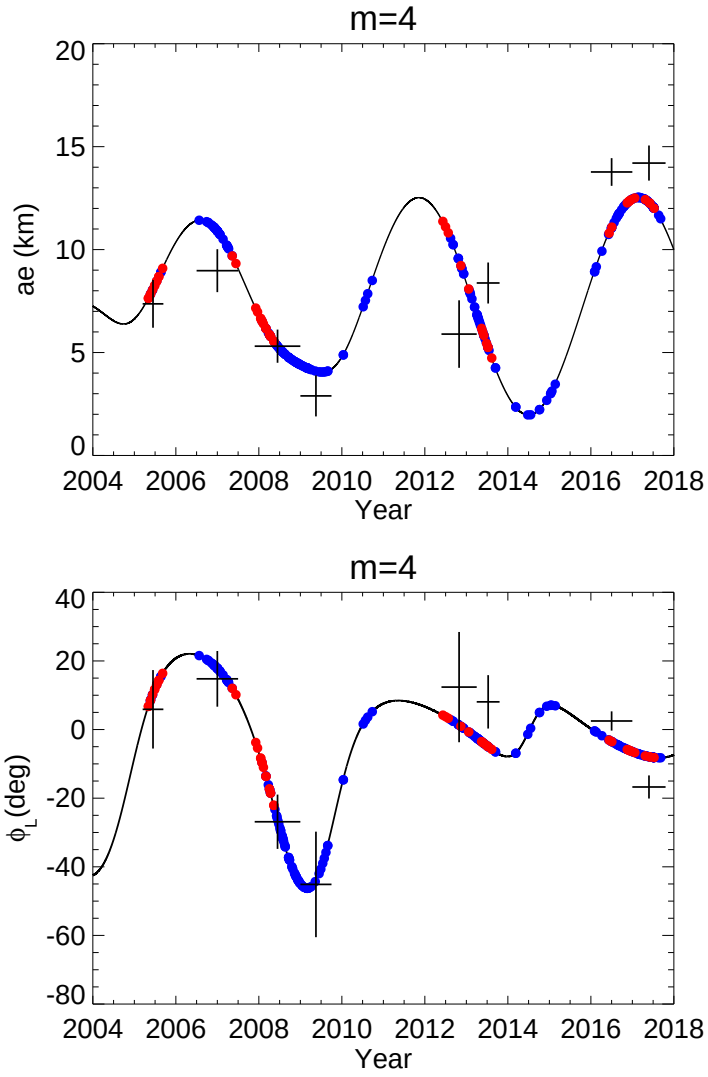

Figure 17. Variation in the amplitude A_4 and phase ϕ_L of the $m = 4$ mode over time incorporating two libration terms with periods of 4.9 and 5.9 yr and amplitudes of 2.8 and 2.6 km, respectively. The model curves match the fitted values for the mode amplitude and libration phase obtained from fits to selected time intervals shown in Fig. 16 reasonably well.

Compared with the reference fit, which uses the same data set, the amplitude, phase and pattern speed of the forced mode due to the Mimas 2:1 ILR are all unchanged, within their stated uncertainties. Our final fit has slightly smaller primary amplitudes for the free $m = 2$, 4 and 5 modes, and slightly larger amplitudes for the $m = 1$ and $m = 3$ modes. The pattern speeds of the free modes are also statistically unchanged, with the exception of the $m = 3$ mode for which Ω_P has decreased by $0.0052 \pm 0.0008^\circ$ d^{-1}.

Libration periods range from 2.25 yr for the $m = 5$ mode to ~ 20 yr for the $m = 3$ mode, but most are in the range of 5–9 yrs. Two of the fitted libration frequencies

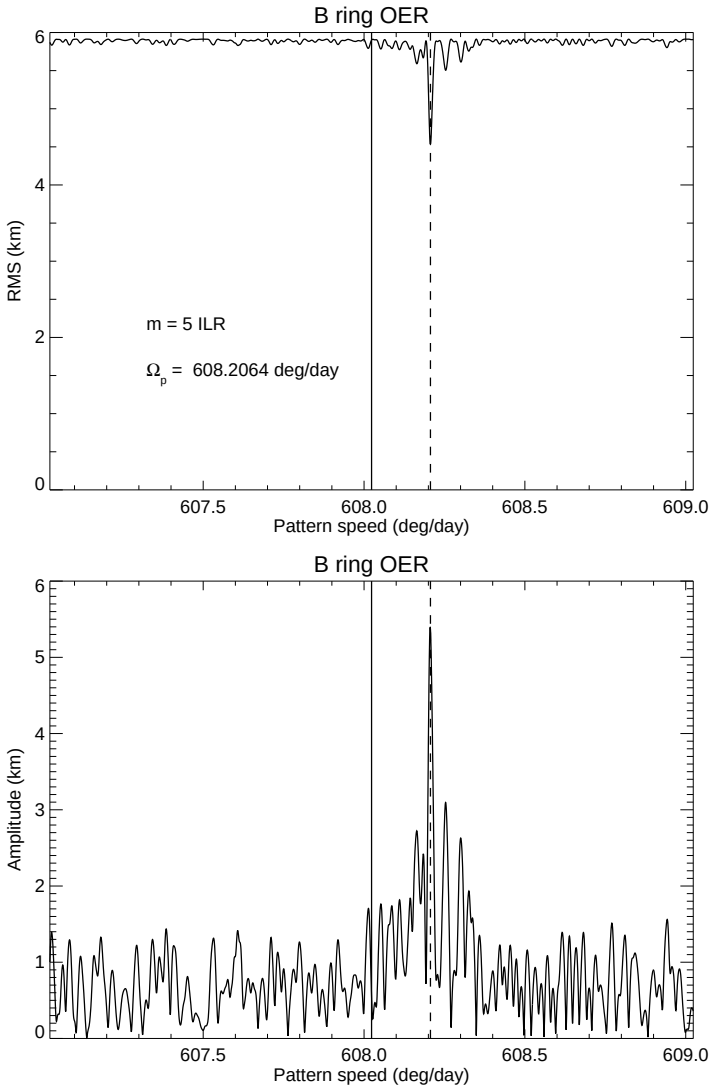

Figure 18. A scan in pattern speed for $m = 5$ normal modes, after removing the signatures of all other modes listed in Table 2. The format is the same as Fig. 3. Here the maximum power is seen at one frequency, at 608.21° d^{-1}, with a radial amplitude of 5.4 km and a minimum $\sigma = 4.5$ km.

are negative, meaning that the corresponding eccentricity vectors rotate clockwise in the $[h, k]$ plane, opposite to the direction of Ω_P, and that $\Omega_1 < \Omega_0$.

Figure 22 shows the mode amplitudes (ae_0 and ae_j), grouped by the value of m. For $m = 2$, the free eccentricity is larger than the forced, implying that the overall $m = 2$ pattern circulates, rather than librates, with respect to the mean longitude of Mimas. With the exception of the $m = 2$ mode, the primary mode amplitudes range from 24 to 5 km while the libration amplitudes lie in the range 2–7 km. Although the primary mode amplitudes generally decrease with increasing m, the latter show no obvious pattern.

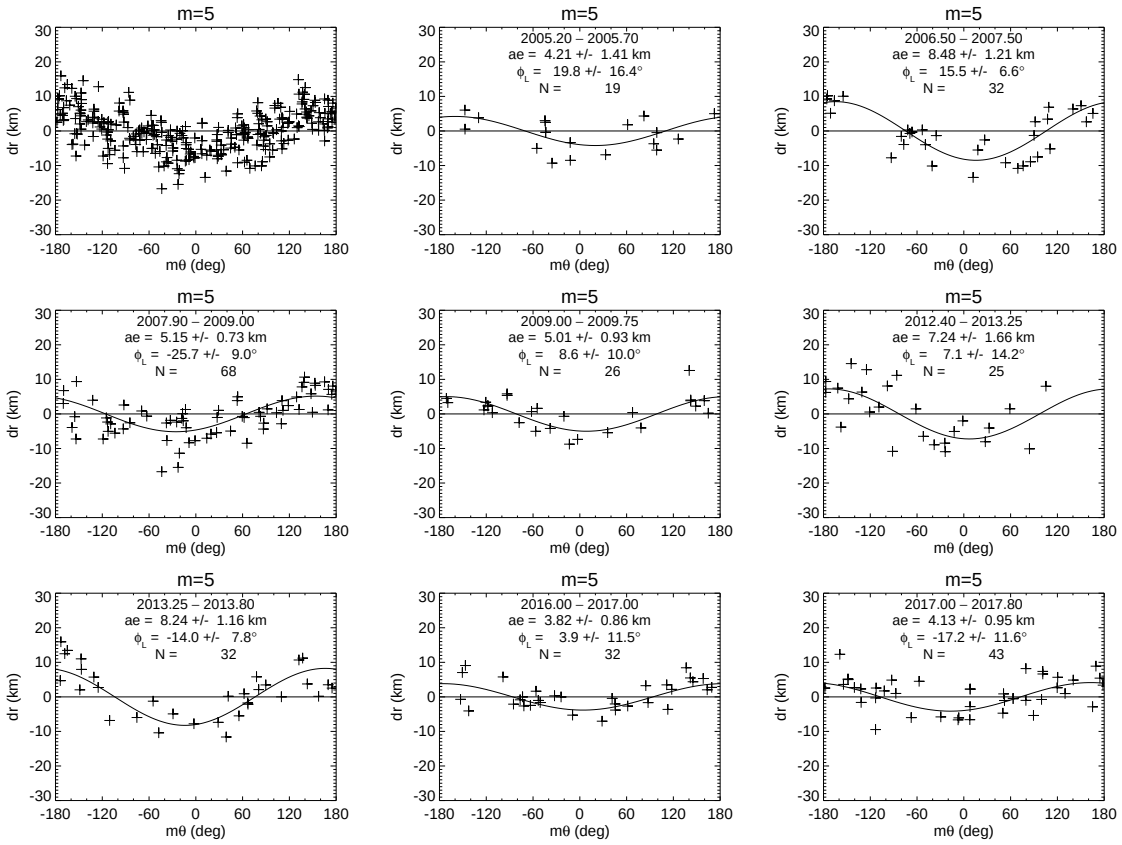

Figure 19. Radius residuals from our final B ring model when the $m = 5$ terms are set to zero, plotted as a function of $m\theta$. The upper left panel shows the full set of observations. The observations are divided into eight different time intervals in the remaining panels, which show modest variations in the amplitude and phase of the $m = 5$ pattern over time. See text for details of the model fit results included in these panels.

Finally, we remind the reader that the relatively long libration periods — in some cases comparable to, or even longer than, the time span of the *Cassini* data — argue for caution in their interpretation. In particular, it is unclear whether the amplitude variations in the modes are truly periodic, or perhaps more irregular in nature.

7. DISCUSSION

7.1. *Resonance cavity model and B ring surface mass densities*

As discussed briefly in Section 2, our model for a librating streamline admits of two distinct dynamical interpretations: one in which a single mode oscillates in amplitude and phase, and the other in which two stable modes with the same value of m and similar pattern speeds interfere to produce a beating pattern. An example of the first case is a mode whose amplitude and phase vary due to a viscous overstability, as originally envisioned by Borderies et al. (1985). In the second case, a ring might support two independent edge modes with the same m but different numbers of radial nodes

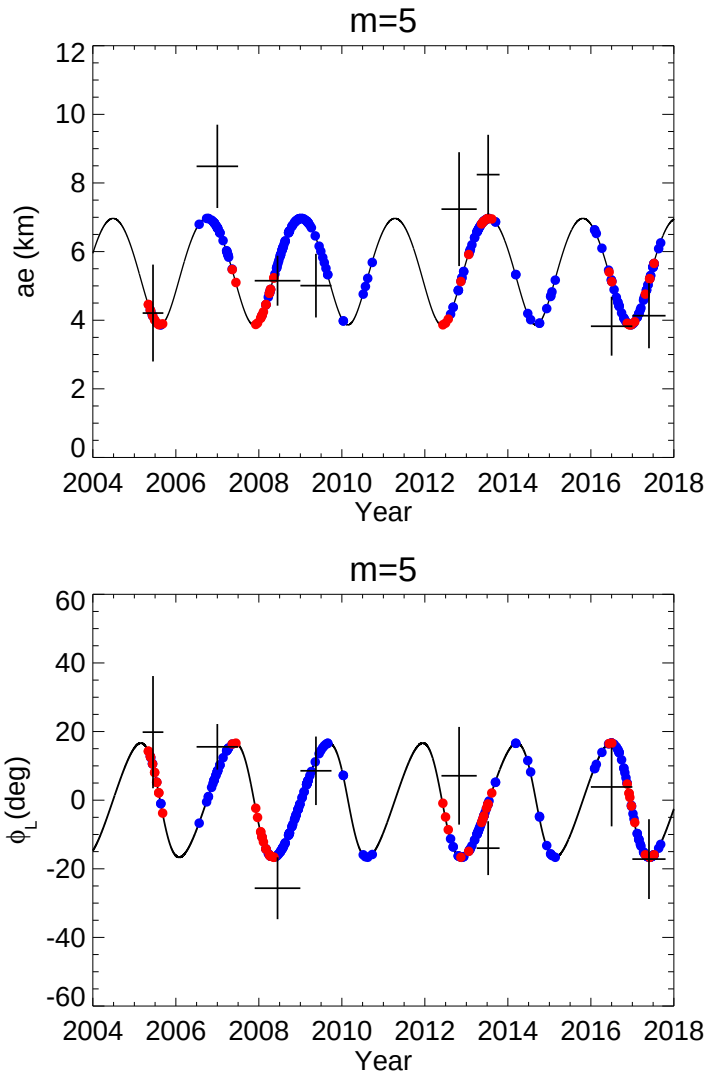

Figure 20. The modeled variation in the $m = 5$ amplitude A_5 and phase ϕ_L, along with fitted values over selected intervals from Fig. 19. The single libration period is 2.26 yr and the amplitude is 1.6 km.

n_r and thus slightly different pattern speeds (Longaretti 2018). Unfortunately, these two situations are indistinguishable when only the shape of a single ring streamline — such as a ring edge — is known, without any information on the radial variation in ring eccentricity.

In the spirit of hypothesis testing, we will assume first that the second interpretation is correct. [**This assumes that we will add an alternative interpretation.**] According to the edge-mode model, as outlined by Spitale and Porco (2010) and French et al. (2016) and reviewed by Nicholson et al. (2018), a normal mode at the edge of a ring with a specified pattern speed Ω_P can be viewed as a pair of free density waves trapped in a resonant cavity between the radius of the corresponding Lindblad resonance $a_{\rm res}$ (where Eq. (2) is satisfied) and the edge of the ring. For an outer ring

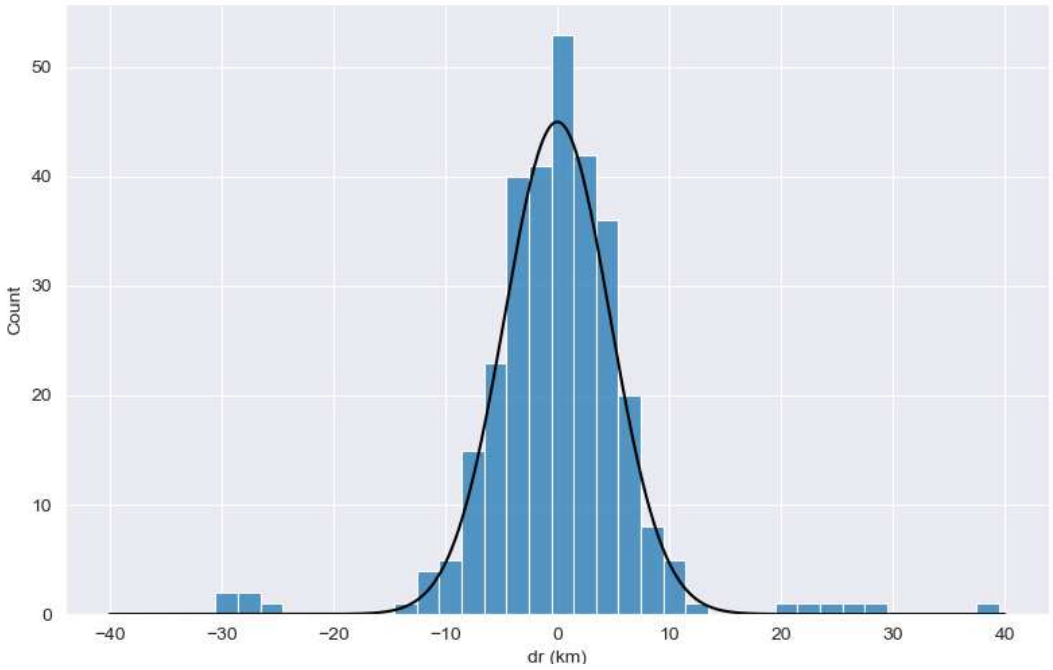

.

Figure 21. Histogram of residuals to the final fit, overplotted with a normal distribution with $\sigma = 4.7$ km. The 11 outlier points with $|dr| > 20$ km were zero-weighted in the fit.

Table 3. Multi-mode fit to *Cassini* data

Parameter	Symbol	Value
mean radius	a(km)	117570.48 ± 0.29
Epoch		UTC 2008 Jan 1 12:00
RMS residual	σ(km)	4.71
# data	N	294
Fit ID		Sa025S-Bring-final_20220111a

			m		
Symbol	1	2	3	4	5
ae (km)	23.56 ± 0.51	33.61 ± 0.45	11.19 ± 0.53	7.32 ± 0.47	5.42 ± 0.44
$\Omega_P(^\circ\ \mathrm{d}^{-1})$	5.0824 ± 0.0012	381.98441 ± 0.00031	507.71325 ± 0.00070	570.52829 ± 0.00084	608.20674 ± 0.00065
$\delta(^\circ)$	64.21 ± 1.87	165.99 ± 0.51	31.00 ± 1.01	9.62 ± 1.34	68.20 ± 1.28
Δa_{res} (km)	-151.03 ± 7.74	-14.70 ± 0.06	-28.14 ± 0.11	-25.93 ± 0.11	-23.47 ± 0.08
ae_1 (km)	4.42 ± 0.63	37.59 ± 0.46	7.41 ± 0.64	2.79 ± 0.47	1.55 ± 0.44
$\Omega_{L,1}(^\circ\ \mathrm{d}^{-1})$	0.1145 ± 0.0096	0.1838 ± 0.0006	[−0.05]	-0.2032 ± 0.0092	0.4353 ± 0.0116
$P_{L,1}$ (yr)	8.609 ± 0.718	5.362 ± 0.017	[19.713]	4.851 ± -0.219	2.264 ± 0.060
$\delta_{L,1}(^\circ)$	193.60 ± 22.47	96.11 ± 1.37	90.97 ± 3.66	57.75 ± 14.00	161.40 ± 23.41
$\Delta a_{1\mathrm{res}}$ (km)	-879.33 ± 12.54	-33.30 ± 0.12	-25.59 ± 0.11	-19.00 ± 0.11	-34.61 ± 0.08
ae_2 (km)	2.84 ± 0.53		2.15 ± 0.49	2.56 ± 0.45	
$\Omega_{L,2}(^\circ\ \mathrm{d}^{-1})$	0.1671 ± 0.0150		0.1342 ± 0.0086	0.1676 ± 0.0095	
$P_{L,2}$ (yr)	5.900 ± 0.529		7.347 ± 0.470	5.881 ± 0.332	
$\delta_{L,2}(^\circ)$	350.70 ± 34.50		247.25 ± 17.50	217.29 ± 13.08	
$\Delta a_{2\mathrm{res}}$ (km)	-1207.61 ± 77.24		-34.97 ± 0.52	-31.64 ± 0.32	

Note:
Values in square brackets [...] were held fixed.

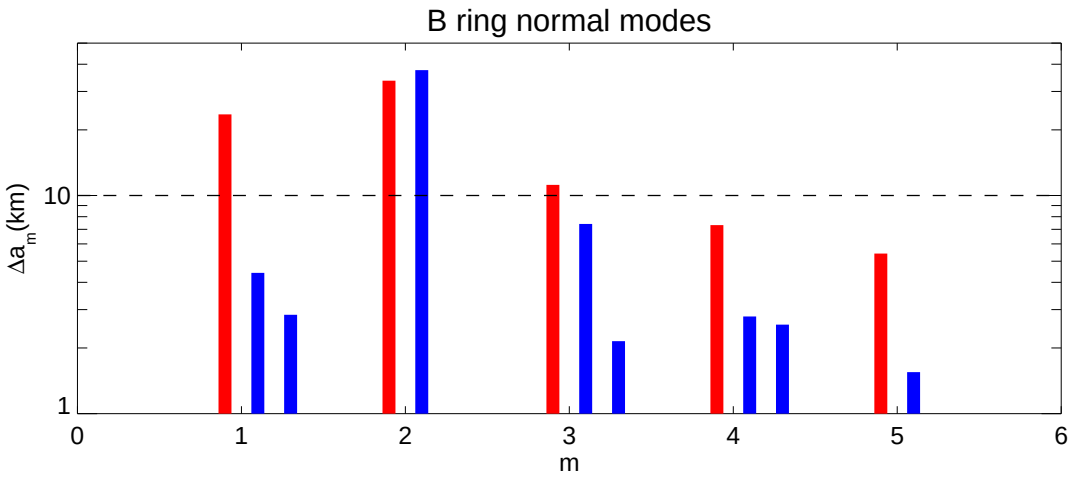

Figure 22. Histogram of fitted normal modes. Red bars represent the principal mode amplitudes ae_0, while blue bars show the amplitudes of the libration terms ae_j. Note that for $m = 2$, ae_1 is larger than ae_0, indicating that the mode is circulating, rather than librating, with respect to Mimas.

edge, an m-armed trailing spiral density wave is generated at the ILR, propagates outwards until it encounters the outer edge of the ring (or the inner edge of a gap), and then reflects as an inward-propagating leading wave. This wave then reflects at the ILR to produce an outward-propagating trailing wave, thus completing the cycle. The angular frequency of the wave $\omega = m\Omega_P$ is determined indirectly via the density wave dispersion relation $\omega(k)$ and the requirement that the total change in phase around each cycle of the cavity is a multiple of 2π.

Under the assumption that each of the libration terms we have identified above is in fact due to beating between the primary normal mode, with pattern speed Ω_P, and a secondary mode with pattern speed $\Omega_{P,j}$, then from Eq. (7) above we have

$$\Omega_{P,j} = \Omega_P + \Omega_{L,j}/m, \tag{13}$$

where $\Omega_{L,j}$ is the fitted libration frequency. (The subscript j allows for the possibility of more than one libration term for a particular value of m, each of which represents a new pattern speed $\Omega_{P,j}$.) Note that if $\Omega_{L,j} < 0$, then $\Omega_{P,j} < \Omega_P$ and the resonant radius of the secondary mode is external to that corresponding to Ω_P. We then calculate the resonance radii $a_{\rm res}$ of these secondary normal modes from their pattern speeds via Eq. (2), as usual, and their distances $\Delta a_{\rm res}$ from the edge of the B ring at 117,570.48 km. The results of this calculation are given in Table 3, based on the libration frequencies determined above, and the resonance locations are plotted in **Fig. 23.**

Once we have $\Delta a_{\rm res}$, Σ can be estimated using the WKB expression for the wavelength of density waves in the vicinity of a Lindblad resonance, leading to the expression (see Section 6.3 of Nicholson et al. (2014a)):

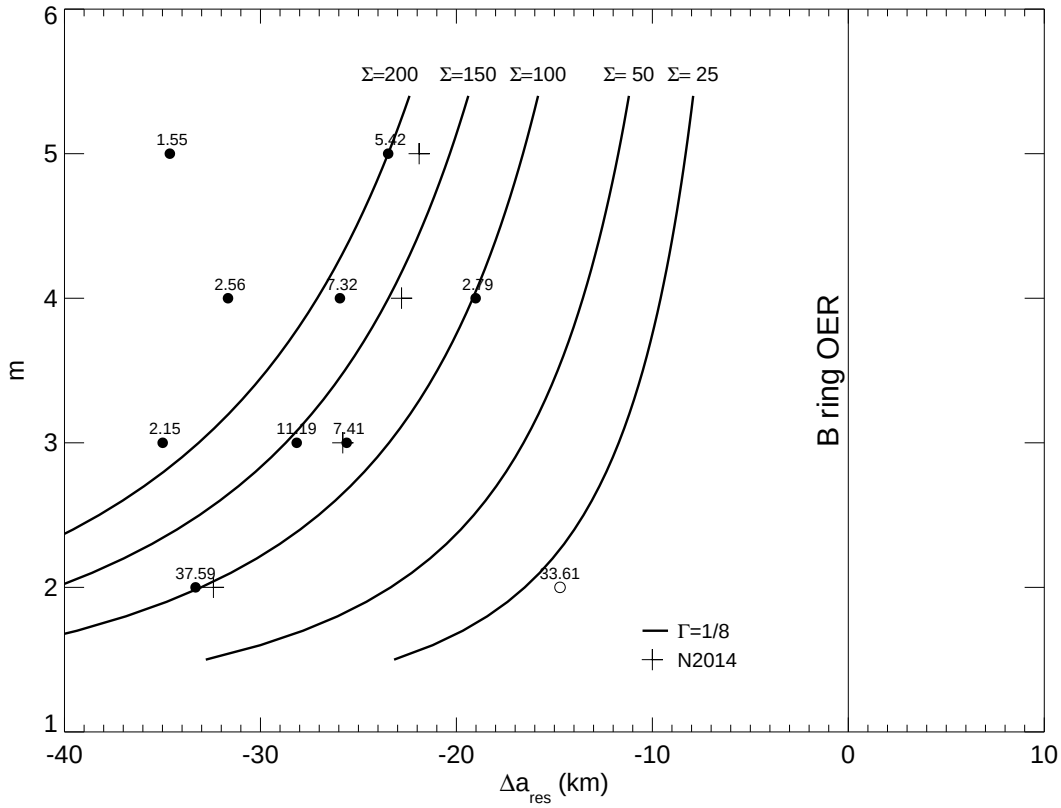

Figure 23. The locations of the calculated resonance radii $a_{\rm res}$ for the normal modes with $m = 2$, 3, 4 and 5 relative to the mean radius of the outer edge of the B ring, 117,570.48 km (see Table 3 for numerical values). Free modes are plotted as filled circles; the open circle marks the $m = 2$ mode forced by Mimas. The solid lines show the predicted $\Delta a_{\rm res}$ as a function of m for nodeless modes ($n_r = 0$) and surface mass densities Σ =25, 50, 100, 150, and 200 g cm^{-2} and $\Gamma = 1/8$ (see text). With the exception of $m = 5$, the lowest-frequency mode for each value of m is more-or-less consistent with $\Sigma \simeq 100$ g cm^{-2}. For the $m = 1$ mode, $\Delta a_{\rm res} = -151$ km and is off scale, reflecting the much longer radial wavelength of density waves with $m = 1$. For comparison, the estimates from Nicholson et al. (2014a) are shown by the + symbols.

$$\Sigma = \left[3(m-1) + \frac{21}{2} J_2 (R/a_{\rm res})^2\right] \frac{M_P \Delta a_{\rm res}^2}{8\pi^2 \Gamma a_{\rm res}^4}, \qquad (14)$$

where M_P, R and J_2 are the mass, equatorial radius and second zonal gravity harmonic of the planet. The numerical factor Γ specifies the number of density wavelengths between the resonant radius and the edge of the ring, where the wave is reflected. A reasonable approximation is to set $\Gamma = (n_r + 1/4)/2$, where n_r is the number of radial nodes of the mode between $a_{\rm res}$ and the edge of the ring and the constant term accounts for a phase change in the density wave when it is reflected at the ILR (S. Tremaine, personal communication). Numerical solutions of the non-linear wave equation by Longaretti (2023) show that the constant term may be closer to 1/16 for an isolated mode, but that inter-mode interactions may lead to an effective value closer to 1/8. For a nodeless mode, then, we have $\Gamma = 1/8$, while for $n_r = 1$, $\Gamma = 5/8$ and for $n_r = 2$ $\Gamma = 9/8$, etc.. Note that, for a given value of n_r and the

Table 4. Normal mode cavities and B ring surface densities

Mode m	n_r [a]	j	A_m (km)	$\Omega_{L,j}$ (° d^{-1})	$\Omega_{P,j}$ [b] (° d^{-1})	$a_{\rm res}$ [c] (km)	$\Delta a_{\rm res}$ [d] (km)	Σ [e] (g cm^{-2})
1	0	0	23.56		5.0824	117419.9	−150.6	30.9
	1	1	4.42	0.1145	5.1969	116691.6	−878.9	216.1
	2	2	2.84	0.1671	5.2495	116364.0	−1206.5	228.8
2	0	1	37.59	0.1838	382.0763	117537.2	−33.3	101.9
3	0	1	7.41	−0.0500	507.6966	117544.9	−25.6	119.5
	1	0	11.19		507.7133	117542.3	−28.1	28.9
	2	2	2.15	0.1342	507.7580	117535.5	−35.0	24.8
4	0	1	2.79	−0.2032	570.4775	117551.5	−19.0	98.7
	1	0	7.32		570.5283	117544.5	−25.9	36.7
	2	2	2.56	0.1676	570.5702	117538.8	−31.7	30.4
5	0	0	5.42		608.2067	117547.0	−23.5	200.3
	1	1	1.55	0.4353	608.2938	117535.9	−34.6	87.1

Notes:
a) Number of radial nodes.
b) Fitted pattern speed: Ω_P for $n_r = 0$ mode and $\Omega_m = \Omega_P + \Omega_{L,j}/m$ for libration components (see Table 3).
c) Calculated resonance radius.
d) Cavity width, based on a mean edge radius of $a_B = 117570.48$ km.
e) Ring surface density (see text).

surface density Σ, the depth of the resonant cavity $\Delta a_{\rm res}$ is greatest for $m = 1$ and decreases as $(m-1)^{-1/2}$ for larger values of the azimuthal wavenumber m. For fixed values of m and Σ, the depth should increase by a factor of $\sim 5^{1/2} = 2.24$ in going from the nodeless mode to $n_r = 1$, and by another factor of $\sim (9/5)^{1/2} = 1.34$ in going from $n_r = 1$ to $n_r = 2$.

To identify the appropriate value of n_r and thus Γ for each mode, we follow Longaretti (2023) and make the simple assumption that, for each value of m, the mode with the smallest value of $\Delta a_{\rm res}$ (*i.e.,* the one whose resonant radius is nearest to the outer edge of the B ring) corresponds to $n_r = 0$, with larger values of $\Delta a_{\rm res}$ being assigned values of $n_r = 1$, 2, etc. Equation (14) is then used to estimate the average surface mass density within the corresponding resonant cavity, with the results listed in **Table 4**. We list here the m-values, the assumed number of radial nodes n_r, amplitudes, pattern speeds, resonance radii and implied surface mass densities Σ for all the normal modes identified in this way.

Several features of these results, however, suggest that our assumption that the observed librations are due multiple normal modes with the same value of m but

varying numbers of radial nodes n_r may be seriously wrong. First is the large scatter in the derived surface mass densities over a relatively small radial range near the B ring's outer edge, ranging from $\sim$ 25 to 230 g cm^{-2}. (These estimates may be compared with the surface mass density in the outer B ring obtained by Hedman and Nicholson (2016) of $\sim 120 - 140$ g cm^{-2}, from the Janus 3:2 resonance near 116,100 km, and the Lissauer et al. (1985) result of 54 g cm^{-2} from the Mimas 4:2 bending wave near 116,500 km, although we note that both results apply to regions 1000 – 1500 km interior to the ring edge.) This scatter might be explained, at least in part, by a rapid increase in surface density within 20-30 km of the ring edge, where most of the very large values of Σ occur, but upon closer inspection this does not seem entirely satisfactory, with very different values being found between $\Delta a_{\rm res} = 25$ and 35 km [5]

A more serious problem is the apparent spacing between modes with different numbers of radial nodes, which is much less than would be expected given the resonance location of the nodeless mode. This mismatch results in the calculated surface densities (except those for $m = 1$) being dramatically lower for $n_r = 1$ or 2 than they are for $n_r = 0$. Choosing larger values of n_r for the secondary modes would just make this problem worse. We have found no plausible solution to this quandary, unless *all* of the modes we have identified have values of $n_r \gg 1$. But in this case, we would need to account for the apparent lack of modes with smaller numbers of radial nodes, which numerical simulations (Longaretti 2023) predict should have larger amplitudes.

This brings us to our third concern: numerical models (Longaretti 2018, 2023) indicate that mode amplitudes should decrease with increasing numbers of radial nodes, or resonance distance from the ring edge, assuming they have similar values of $q_{\rm max}$, the maximum dimensionless eccentricity gradient. This is also inconsistent with our results in Fig. 23, although it is possible that inter-mode coupling through the ring's self-gravity could induce oscillations in their amplitude, resulting in some modes being unusually weak at certain times (Longaretti 2023).

For a theoretical analysis of the dynamics of normal modes in this region of the B ring, including a discussion of the possibility that the observed librations arise instead from viscous overstability and/or mutual interactions between modes with differing values of m, we refer the interested reader to the companion (?) paper by Longaretti (2023). This work includes a sequence of nonlinear simulations of edge modes with $1 \leq m \leq 5$ and $0 \leq n_r \leq 2$, for an assumed value for the ring surface mass density Σ, that is adjusted in an attempt to fit the observed mode amplitudes and resonant cavity widths presented in Table 3. In addition to the conclusion that there is no self-consistent multi-mode model that fits the observations, one outcome of these models is the realization that the mode amplitudes A_m are coupled to the surface

[5] In the case of the $m = 1$ modes, for which the secondary modes associated with the libration frequencies $\Omega_{L,1}$ and $\Omega_{L,2}$ yield much larger values of Σ, the problem might be due to our assumption that $n_r = 1$ and 2 as $\Sigma \sim \Delta a_{\rm res}^2/n_r$ if $n_r \gg 1$.

mass density of the ring through the maximum allowed value for the dimensionless eccentricity gradient within the rings, $q \simeq ade/da$ being ≤ 0.8. Amplitudes for the primary (*i.e.,* nodeless) $m = 2$ and $m = 3$ modes can only be as large as the observed values in Table 4 if Σ is of order 200 g cm^{-2}, at least in the outer 20-30 km of the B ring. Smaller mass densities in this region lead to shorter radial wavelengths and unacceptably large values of q, for the same value of A_m. The primary $m = 1$ mode, on the other hand, with its much wider resonant cavity, can be fit fairly well with an average value of $\Sigma \simeq 60$ g cm^{-2}, more compatible with published estimates based on density and bending waves (see above)..

[**Should we say more here, such as mentioning PYL's predicted mode amplitudes and cavity widths, or defer this whole discussion to his paper and simply reference it here?**]

7.2. *Phase offset relative to Mimas*

In our reference fit to the *Cassini* data set in Table 2, the first $m = 2$ component represents the forced perturbation due to the Mimas 2:1 ILR. This part of the overall model thus contains the primary information on the response of the streamlines at the edge of the B ring to the forcing by the resonance, including any offset in the phase of the response relative to the forcing function. The latter is a predicted consequence of collisional dissipation within the ring, and the size of the phase lag is related to the effective viscosity of the rings (Borderies et al. 1982). Moreover, the amplitude of the torque exerted by Mimas on the rings due to the 2:1 resonance is also dependent on this phase lag (Tajeddine et al. 2017; Longaretti 2018). Previous investigations have yielded somewhat inconsistent results on the phase lag at the edge of the B ring, ranging from $2.9 \pm 0.3°$ (Spitale and Porco 2010) to $0.7 \pm 1.1°$ in longitude (Nicholson et al. 2014a). In both cases, one of the two minima in ring radius was found to lag behind the mean longitude of Mimas at the epoch of the fit. In this section we compare both the pattern speed and phase of the $m = 2$ forced perturbation to previous results and to that expected from dynamical theory.

We first compare the measured pattern speed of the forced component of the $m = 2$ mode with the mean angular velocity of Mimas, as these are expected to be equal (Goldreich and Tremaine 1978; Porco et al. 1984). The upper panel of **Fig. 24** compares the best-fitting pattern speed $\Omega_P = 381.98430 \pm 0.00045°$ d^{-1} of this mode from our reference fit in Table 2 with the actual mean motion of Mimas during the period of the *Cassini* mission, obtained by evaluating the epicyclic orbital elements [6] for the numerical ephemeris, SAT441 (Acton, C. H. 1996). Complicating this com-

[6] The epicyclic elements are analogous to the usual osculating Keplerian orbital elements, but take into account the zonal gravity coefficients of the planet (J_2, J_4, etc.) that have the effect of modifying Kepler's third law and introducing precession of both the apsidal line and the nodes of eccentric or inclined orbits. See Renner and Sicardy (2006) for further details and conversion formulae from osculating to epicyclic elements.

parison is the fact that Mimas itself is in a 4:2 inclination resonance with the satellite Tethys, which leads to long-term periodic variations in the former's longitude, and thus in its mean motion. The libration period of the Mimas-Tethys resonance is $P_L = 70.8$ yr and the corresponding variations in Mimas's mean longitude have an amplitude of $\Theta_L = 43.7°$ (Harper and Taylor 1993). As a result, the satellite's mean motion varies periodically by up to $2\pi\Theta_L/P_L = 0.0106°$ d^{-1}. The long-term average value of $n_{\rm Mimas}$ is 381.994509° d^{-1}, but in the early part of the *Cassini* mission it was $\sim$ 381.9835° d^{-1}, near its minimum value (Nicholson et al. 2014a). The long-term trend in Mimas's mean motion seen in Fig. 24 is a consequence of this slow variation. In addition to the long-term trend, there is a shorter-term variation in the epicyclic mean motion with a period of 0.62 yr and an amplitude of $\pm 0.005°$ d^{-1} that is associated with the nearby 2:1 Lindblad resonance with Tethys (Vienne and Duriez 1995). These variations in the mean motion of Mimas make an instantaneous comparison with the fitted pattern speed of the forced $m = 2$ perturbation rather tricky, but Fig. 24 shows that the best-fitting pattern speed is indeed very close to the average mean motion of Mimas during the period of our observations.

Having established that the forced $m = 2$ mode closely tracks the average mean motion of Mimas, the next step is to measure the offset in phase between the radial minimum of the mode and the average longitude of Mimas. This is also complicated by the effects of the Mimas-Tethys resonance. We make the working assumption that the ring is able to follow the slow librational motion of Mimas's longitude, but not the short-period variations in its true or instantaneous longitude. Our approach therefore is to remove the short-period variations by subtracting from the epicyclic mean longitude a linear term with a rate of 381.9842959° d^{-1}, as determined from our reference fit in Table 2. The lower panel in Fig. 24 compares the fitted phase of the forced $m = 2$ mode, which uses this same pattern speed, with Mimas's detrended orbital longitude from the numerical ephemeris. In addition, a constant offset equal to Mimas's epicyclic mean longitude at our reference time of 2008 Jan 1 12:00 UTC, or 347.21996°, has been subtracted from both the Mimas longitudes and the fitted $m = 2$ phase. (The short vertical line marks this epoch. By construction, the detrended Mimas mean longitude is exactly zero at our reference time, although the long-period resonant variations are still apparent, especially after 2015.) The best-fitting value of the phase lag from the reference fit in Table 2 is $-0.39 \pm 0.73°$ relative to the epicyclic longitude of Mimas at the reference time, as shown by the horizontal blue line in Fig. 24. If instead we use our final fit from Table 3, for which $\delta = 346.10 \pm 0.59°$, we find an offset of $-1.12 \pm 0.59°$ relative to Mimas. These results are consistent with the less-precise phase lag of $-0.7 \pm 1.1°$ found by Nicholson et al. (2014a), but somewhat smaller in magnitude than that obtained by Spitale and Porco (2010), viz. $-2.3 \pm 0.3°$.

Given the departures of Mimas's epicyclic longitude from any constant-rate model, one might ask if there is a better way to measure the true phase offset. One alternative is to use the actual epicyclic mean longitude of Mimas in the orbit fitting program, instead of the linear term in Eq. (1), and then solve for a constant offset with respect to this, which we refer to as $\delta\lambda$. (This was the approach followed by Nicholson et al. (2014a).). We have repeated both our reference fit in Table 2 and our final fit (Table 3) with this modification. We find that $\delta\lambda = -0.51 \pm 0.56°$ and $-1.28 \pm 0.38°$, respectively. Within their uncertainties, all four estimates of the phase lag are reasonably consistent and imply a small negative offset in the longitude of one minimum of the forced $m = 2$ mode relative to the mean epicyclic longitude of Mimas. As discussed in Nicholson et al. (2022), such a phase lag in the radial minimum is consistent with a gravitational torque between Mimas and the rings that acts to remove excess angular momentum from the B ring and transfers it to the satellite. But we must caution the reader that the measured phase lag is only barely statistically significant, and might also be subject to significant temporal variations associated with the observed mode librations (Longaretti 2018).

Should we discuss the theoretical situation here? Longaretti (2023) estimate the ring viscosity, far from the edge, that is implied by our measured lag, and compare this with estimates of the viscosity due to self-gravity wakes.

7.3. *Resonant confinement of the B ring*

How much should we add here? Longaretti (2023) shows that the distance of the Mimas 2:1 ILR from the B ring edge controls the torque Mimas exerts on the ring, and can be combined with the measured phase lag to obtain an independent estimate of the ring viscosity. Also, what about the forced amplitude $ae = 33.6$ km at the edge, which is also predicted by Longaretti (2023) and involved in the calculated torque balance? I am uneasy about saying too much about this, when it would just amount to paraphrasing what is in PYL's paper and is a pretty complicated argument that depends on his prior theoretical development. Perhaps PYL can suggest a few sentences here, summarizing his results and referring to his paper? – PDN

8. CONCLUSIONS AND OPEN QUESTIONS

This section has yet to be revised as of Jan 15, 2023 and was mostly written in Jan 2022. – pdn I have restored the Questions we had posed for PYL to consider, and his answers.

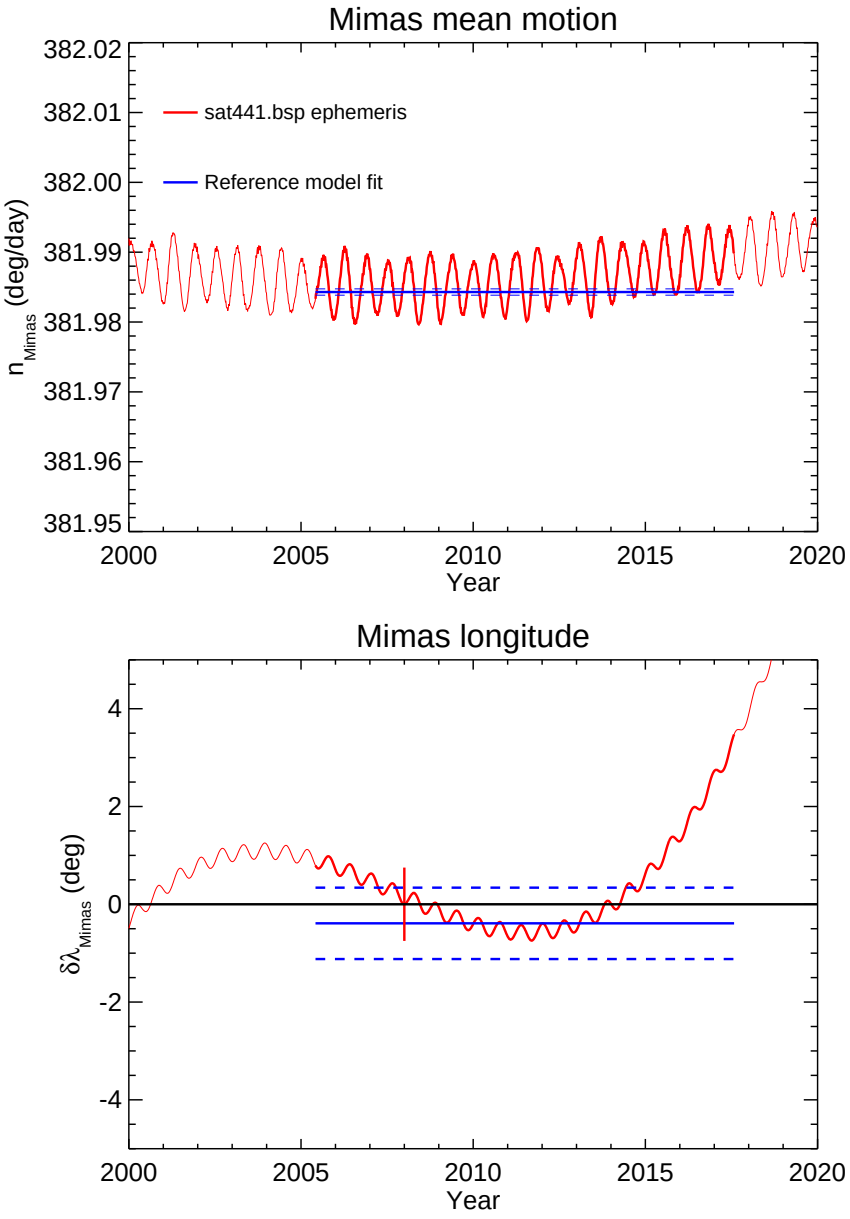

.

Figure 24. (Upper panel) A comparison of the fitted pattern speed of the forced $m = 2$ mode with the actual mean motion of Mimas obtained by evaluating the epicyclic orbital elements from the numerical ephemeris SAT441. The horizontal lines show the fitted pattern speed and error bars for the forced mode, Ω_P from our reference fit in Table 2, while the oscillatory curve is from the satellite ephemeris. (Lower panel) A comparison of the fitted phase δ of the forced $m = 2$ mode from the reference fit with the mean longitude of Mimas at $t = t_0$ derived from the ephemeris. The horizontal line with error bars shows the mode phase relative to Mimas's mean longitude at our reference epoch, while the oscillatory curve is again from the satellite ephemeris. The latter has had a linear trend removed with a slope equal to the best-fitting mode pattern speed shown in the upper panel, and both the mode phase and detrended Mimas longitudes are calculated relative to the mean epicyclic longitude of Mimas at $t = t_0$. The short vertical line marks the epoch of the fitted orbital elements, when the measured phase lag was $-0.39 \pm 0.73°$. In both panels, the curves computed from the satellite ephemeris are plotted as heavier lines during the actual period of *Cassini* observations used in the fits.

- The dominant $m = 2$ mode is observed to circulate with a period of 5.36 yr and an amplitude that varies from a minimum of 4 km to a maximum of 71 km. Under the assumption that this is due to a combination of a resonantly-forced perturbation by Mimas plus an $m = 2$ normal mode (Spitale and Porco 2010; Nicholson et al. 2014a), we find $\Delta a_{\rm res} = -14.7$ km and $A_m = 33.6$ km for the forced mode, while $\Delta a_{\rm res} = -33.3$ km and $A_m = 37.6$ km for the free mode. **Question:** Why are the two modes of almost equal amplitude? Perhaps some sort of limit on $q = ade/da$? **PY: See my comments in relation to figure 23. This is coincidental in the interpretation of your results given there. Note that this coincidence is bound to happen, as amplitudes vary. The problem is that we just happen to look at the right moment (somewhat like a stopped clock being right twice a day). This may happen. This is obviously falsifiable. I may derive a typical time-scale of amplitude variation if I find the time, so that we can estimate how long such a coincidence may last... The problem is that we will not be looking again at the Saturnian system at the right time to check this...**

- Additional modes are seen with $m = 1$, 3, 4 and 5 and amplitudes of ~ 24, 11, 7 and 5 km, respectively. We interpret these as normal modes trapped in resonant cavities at the edge of the B ring. From their observed pattern speeds, we calculate resonant locations with respect to the mean edge ranging from $\Delta a_{\rm res} = -151$ km ($m = 1$) to -23 km ($m = 5$). **Question:** Why are these particular modes excited? Are they connected to the dominant $m = 2$ mode? **PY: Ok. Best guess (always the same): ALL modes should be overstably excited. Now, as I said earlier, they undergo phases of growth and phases of decay. This being said, there might be two reasons why we see some and not others: (1) the ones we do not see may happen to have too small amplitudes at the moment of observation, due to their varying amplitudes due not only to phases of growth an decay, but also to mode coupling. (2) mode coupling and initial conditions may have resulted in some modes never being able to reach a detectable amplitude.**

- It appears all of the modes with $m = 1$, 3, 4 and 5 librate in amplitude and phase, and — except for $m = 5$ — there appear to be at least *two* libration terms for each value of m. Libration amplitudes range from 1.6 to 7.4 km, and periods $2\pi/P_L$ range from 2.3 to ~ 20 yr. From the shape of the ring edge alone, we cannot discriminate between three possible dynamical scenarios: (1) they represent true physical librations of nodeless normal modes, with the same radial structure; (2) they are 'apparent' librations due to the beating of independent normal modes with the same m but different numbers of radial

nodes; or (3) their changing amplitude and phase on decadal timescales is a consequence of non-linear coupling between excited modes of different m.

- Given the large amplitude of the $m = 2$ mode(s), and the resulting value of q in the outer B ring, one might expect the existence of overtone modes, with perturbations varying as an n-tuple of $m[\lambda - \Omega_P(t - t_0) - \delta]$. Such distortions should look like normal modes with $m' = nm$ but the same pattern speed Ω_P. A search has not revealed any evidence for such modes with $m = 4$ or $m = 6$ and $\Omega_P = \Omega_2$.

- The overall RMS residual of our best fit is 4.7 km, which is still at least 10 times larger than the uncertainties in the measured radii, and much greater than the RMS for fits to other sharp-edged features in the nearby Cassini Division (French et al. 2016). Is this due to unmodeled modes of oscillation, to more localized distortions such as those seen in some ISS images (Spitale and Porco 2010; Hedman and Nicholson 2019), or to something else? **PY: On this point, I have asked myself if a mess of smaller amplitude stuff, either other free modes modes or remaining small amplitude but decaying librations (as per the picture described earlier) could not result, for each m, in a very complex time-dependent pattern, making it impossible to analyze simply, each contribution being individually too small to produce a convincing identification in your scanning procedure. Not sure what this idea is worth though.**

- Our analysis of the forced component of the $m = 2$ mode, and that of Spitale and Porco (2010), indicate that one minimum of the radial pattern *lags behind* the mean longitude of Mimas by $1 - 2°$. A more accurate estimate is made difficult by the various long-term perturbations in the orbit of Mimas due to the 4:2 vertical resonance with Tethys ($P_L = 70$ yr) and the nearby 2:1 Lindblad resonance ($P_L = 0.62$ yr), but the sign of the lag is consistent with the expectation that Mimas is removing angular momentum from the B ring at the 2:1 resonance, and thus preventing it from spreading due to viscous interactions.

9. ACKNOWLEDGEMENTS

This work was supported in part by the Cassini project and by NASA CDAP grants NNX09SE66G and 80NSSC10K0890. P.Y.L. acknowledges support by the French National Program of Planetology (PNP). We are especially grateful to Aseel Anabtawi for her leadership of the *Cassini* RSS Operations Team, and to the staff of the NASA DSN and ESA ground stations for their superb support, both of which contributed to the successful two-way RSS occultation experiments used for this work.

10. DATA AVAILABILITY

Most of the occultation data from which our results were obtained are publicly available from NASA's Planetary Data System Ring-Moon Systems Node at `https://pds-rings.seti.org/ringocc/`. Raw observations of all other observations are available from the PDS Atmospheres Node at `https://pds-atmospheres.nmsu.edu/`. Specially-processed data used for this work are available upon request from the lead author.

REFERENCES

Acton, C. H. 1996. Ancillary data services of NASA's Navigation and Ancillary Information Facility. 1996. Planetary and Space Science, 44, 65-70.

Borderies, N., Goldreich, P., Tremaine, S. 1982. Sharp edges of planetary rings. Nature 299, 209.

Borderies, N., Goldreich, P., Tremaine, S. 1983a. The variations in eccentricity and apse precession rate of a narrow ring perturbed by a close satellite. Icarus 53, 84-89.

Borderies, N., Goldreich, P., Tremaine, S. 1983b. The dynamics of elliptical rings. The Astronomical Journal 88, 1560-1568.

Borderies, N., Goldreich, P., Tremaine, S. 1985. A granular flow model for dense planetary rings. Icarus 63, 406–420.

Colwell, J. E., Nicholson, P. D., Tiscareno, M. S., Murray, C. D., French, R. G., Marouf, E. A. 2009. The structure of Saturn's rings. In "Saturn after Cassini-Huygens." M. Dougherty & S. Krimigis, Eds., Springer. 375-412.

Colwell, J. E., Cooney, J. H., Esposito, L. W., Sremčević, M. 2009. Density waves in Cassini UVIS stellar occultations. 1. The Cassini Division. Icarus 200, 574-580.

El Moutamid, M., and 7 colleagues 2015. An analysis of the A ring's outer edge probes Saturn's interior. AAS/Division for Planetary Sciences Meeting Abstracts #47 104.05.

El Moutamid, M., Nicholson, P. D., French, R. G., Tiscareno, M. S., Murray, C. D., Evans, M. W., French, C. M., Hedman, M. M., Burns, J. A. 2016. How Janus' orbital swap affects the edge of Saturn's A ring? Icarus 279, 125-140.

Esposito, L. W., Cuzzi, J. N., Holberg, J. B., Marouf, E. A., Tyler, G. L., Porco, C. C. 1984. Saturn's rings - Structure, dynamics, and particle properties. Saturn 463-545.

French, R. G., Nicholson, P. D., Porco, C. C., Marouf, E. A. 1991. Dynamics and structure of the Uranian rings. Uranus 327.

French, R. G., Marouf, E. A., Rappaport, N. J., McGhee, C. A. 2010. Occultation observations of Saturn's B ring and Cassini Division. The Astronomical Journal 139, 1649-1667.

French, R. G., Nicholson, P. D., McGhee-French, C. A., Lonergan, K., Sepersky, T., Hedman, M. M., Marouf, E. A., Colwell, J. E. 2016. Noncircular features in Saturn's rings III: The Cassini Division. Icarus 274, 131-162.

French, R. G., McGhee-French, C. A., Lonergan, K., Sepersky, T., Jacobson, R. A., Nicholson, P. D., Hedman, M. M., Marouf, E. A., Colwell, J. E. 2017. Noncircular features in Saturn's rings IV: Absolute radius scale and Saturn's pole direction. Icarus 290, 14-45.

Goldreich, P., Tremaine, S. D. 1978. The formation of the Cassini Division in Saturn's rings. Icarus 34, 240-253.

Harper, D., Taylor, D. B. 1993. The orbits of the major satellites of Saturn. Astronomy and Astrophysics 268, 326.

Hedman, M. M., Nicholson, P. D., Baines, K. H., Buratti, B. J., Sotin, C., Clark, R. N., Brown, R. H., French, R. G., Marouf, E. A. 2010. The architecture of the Cassini Division. Astron. J. 139, 228-251.

Hedman, M. M., Nicholson, P. D. 2016. The B-ring's surface mass density from hidden density waves: Less than meets the eye? Icarus 279, 109-124.

Hedman, M. M., Nicholson, P. D. 2019. Axisymmetric density waves in Saturn's rings. Monthly Notices of the Royal Astronomical Society 485, 13-29.

Kirkwood, D. 1866. On the theory of meteors. Proc. Am. Assoc. Adv. Sci. for 1866, 8–14

Lissauer, J. J., Goldreich, P., Tremaine, S. 1985. Evolution of the Janus-Epimetheus coorbital resonance due to torques from Saturn's ring. Icarus 64, 425.

Longaretti, P.-Y. Theory of narrow rings and sharp edges. Planetary Ring Systems: Properties, Structure, and Evolution. Cambridge University Press, 225-275.

Longaretti, P.-Y. Stationary dynamics of planetary ring edge modes. I Saturn's B edge. (to be submitted).

Longaretti, P.-Y., Rappaport, N. 1995. Viscous overstabilities in dense narrow planetary rings. Icarus 116, 376-396.

Marouf, E. A., Tyler, G. L., Rosen, P. A. 1986. Profiling Saturn's rings by radio occultation. Icarus 68, 120.

Murray, C. D., & Dermott, S. F. 1999, Solar System Dynamics (Cambridge University Press)

Nicholson, P. D., Cooke, M. L., Pelton, E. 1990. An absolute radius scale for Saturn's rings. Astron. J. 100, 1339-1362.

Nicholson, P. D., French, R. G., Hedman, M. M., Marouf, E. A., Colwell, J. E. 2014a. Noncircular features in Saturn's rings: I. The edge of the B ring. Icarus 227, 152-175.

Nicholson, P. D., French, R. G., McGhee-French, C. A., Hedman, M. M., Marouf, E. A., Colwell, J. E., Lonergan, K., Sepersky, T. 2014b. Noncircular features in Saturn's rings: II. The C ring. Icarus 241, 373-396.

Nicholson, P. D., De Pater, I., French, R. G., Showalter, M. R. 2018. The rings of Uranus. Planetary Ring Systems: Properties, Structure, and Evolution. Cambridge University Press, 93-111.

Nicholson, P. D., French, R. G., and 11 colleagues 2022. The seven-lobed shape of the outer edge of Saturn's A ring. Icarus (in press).

Porco, C., Danielson, G. E., Goldreich, P., Holberg, J. B., Lane, A. L. 1984. Saturn's nonaxisymmetric ring edges at 1.95 R(s) and 2.27 R(s). Icarus 60, 17-28.

Porco, C. C., and 34 colleagues 2005. Cassini Imaging Science: Initial results on Saturn's rings and small satellites. Science 307, 1226-1236.

Renner, S., Sicardy, B. 2006. Use of the geometric elements in numerical simulations. Celestial Mechanics and Dynamical Astronomy 94, 237.

Schinder, P. J., and 6 colleagues 2015. A numerical technique for two-way radio occultations by oblate axisymmetric atmospheres with zonal winds. Radio Science 50, 712.

Spitale, J. N., Porco, C. C. 2009. Time variability in the outer edge of Saturn's A-ring revealed by Cassini imaging. The Astronomical Journal 138, 1520-1528.

Spitale, J. N., Porco, C. C. 2010. Detection of free unstable modes and massive bodies in Saturn's outer B ring. The Astronomical Journal 140, 1747-1757.

Tajeddine, R., Nicholson, P. D., Longaretti, P.-Y., El Moutamid, M., Burns, J. A. 2017. What confines the rings of Saturn? The Astrophysical Journal Supplement Series 232, 28.

Tiscareno, M. S., Harris, B. E. 2018. Mapping spiral waves and other radial features in Saturn's rings. Icarus 312, 157-171.

Vienne, A., Duriez, L. 1995. TASS1.6: Ephemerides of the major Saturnian satellites. Astron. Astrophys. 297, 588-605.

Yoder, C. F., Synnott, S. P., Salo, H. 1989. Orbits and masses of Saturn's co-orbiting satellites, Janus and Epimetheus. The Astronomical Journal 98, 1875.